

POLITECNICO DI TORINO

Dipartimento di Ingegneria Meccanica e Aerospaziale
Corso di laurea magistrale in Ingegneria Aerospaziale

Tesi di Laurea Magistrale



Main Structural Design Considerations for Reusable Launch Vehicles

Relatore:

Prof. Erasmo Carrera

Candidato:

Davide Boiani

Correlatori:

Prof. Alfonso Pagani

Ing. Rodolfo Azzara

Aprile 2021

*Ai miei genitori
con tantissimo affetto*

Imagination will often carry
us to worlds that never were,
but without it we go nowhere.

Carl Sagan

Contents

List of Figures	III
List of Tables	VII
Abstract	IX
Introduction	1
1 Launch Vehicles and the Chances for Reusability	3
1.1 Reusable Launch Vehicles	7
2 Design of Thin-Walled Shell Space Structures	11
2.1 Introduction	12
2.1.1 General Design Considerations	13
2.2 Stiffening Techniques and NASA Testing Campaign	17
2.2.1 Results for Orthogrid Stiffened Shell	18
2.3 Launch Loads	23
3 Key Problems in the Structural Design of RLVs	29
3.1 Types of Reusable Launch Vehicles	30
3.1.1 Vertical Takeoff-Vertical Landing RLVs	31
3.1.2 Vertical Takeoff-Horizontal Landing RLVs	35
3.1.3 Technological Comparisons	37
3.2 Considerations on Design Parameters	41
3.3 Primary Vehicle Structures	43
3.4 Reusable Cryogenic Tanks	47
3.4.1 Aluminum-Lithium Cryogenic Tanks	47
3.4.2 Composite Cryogenic Tanks	50

3.5	Thermal Protection and Insulation Systems	53
3.5.1	TPS Materials Research Programs	55
4	The Carrera Unified Formulation for Nonlinear Problems	61
4.1	Fundamental Relations	64
4.1.1	Hooke's Law	65
4.2	Finite Element Approximation	68
4.3	Nonlinear Equilibrium Equations	71
4.3.1	Newton-Raphson linearization with path-following constraint	72
5	Examples of Nonlinear Problems using the <i>MUL</i>² Software	75
5.1	1D Structures Analyses	76
5.1.1	Geometric Nonlinearities in a Beam Structure	77
5.1.2	Post Buckling in a Beam Structure	79
5.2	2D Structures Analyses	81
5.2.1	Modal Analysis of a 2D Plate	81
5.2.2	Nonlinear Analysis of a Shell Structure	82
5.2.3	Pinched Semi Cylindrical Shell	84
6	Conclusions and Recommendations	87

List of Figures

1.1	Launch of the Saturn V during the Apollo 11 mission	4
1.2	A Soyuz rocket taking off from Baikonur Cosmodrome, KZ	5
1.3	The Ariane 5 launch vehicle (Fig. 1.3a) and the Vega launch vehicle (Fig. 1.3b). <i>Courtesy of ESA</i>	6
1.4	The Space Shuttle (Fig. 1.4a) and the X-33 concept (Fig. 1.4b)	7
1.5	The SpaceX family of reusable Launch Vehicles	9
1.6	The Blue Origin family of reusable Launch Vehicles	9
2.1	Examples of shells buckling under compressive loads	12
2.2	The knockdown factor on the load-displacement curve [2]	14
2.3	Global and local buckling loads (unstiffened cylinder, right), diamond- shaped dimple (left) [2]	15
2.4	The Single Perturbation Load Approach diagram [2]	15
2.5	Empirical KDFs lower-boundary curves for cylindrical shells as a function of R/t [2]	16
2.6	Stiffening techniques used in [4]	17
2.7	Measured geometric imperfections in inches (blue and red contours correspond to inward and outward radial imperfections, respectively)	18
2.8	Cylindrical Coordinate System	18
2.9	Predicted and measured load versus end-shortening response curves	19
2.10	Measured prebuckling (point a), incipient buckling (point b), and postbuckling (point c) radial displacements	21
2.11	Predicted prebuckling, incipient buckling, and postbuckling radial displacements	22
2.12	Falcon 9 and Falcon Heavy payload design load factors [8]	24

2.13	Example of Falcon 9 maximum predicted environment, both from Cape Canaveral and Vandenberg Base [8]	26
3.1	Typical mission profile for the future Blue Origin New Glenn rocket [11]	32
3.2	Typical mission profile for a SpaceX Falcon 9 rocket [8]	32
3.3	Typical mission profile for a SpaceX Falcon Heavy rocket [8]	33
3.4	Structural model for a preliminary hydrogen RLV [12]	34
3.5	Sketch of a sample In-Air-Capturing mission profile [10]	36
3.6	Size and architecture of some conceptual VTVL and VTHL RLVs compared to Falcon 9 and Ariane 5 [10]	37
3.7	Mass comparison between the aforementioned conceptual RLVs [10]	38
3.8	Inert Mass and Structural Indices of the conceptual first stages compared [10]	39
3.9	Reentry trajectories and heat flux estimation for various reusable solutions, including Falcon 9 [10]	40
3.10	Sketch of an intertank structure. <i>Courtesy of NASA</i>	43
3.11	Falcon 9 thrust structure and engines. <i>Courtesy of SpaceX</i>	43
3.12	Aluminum-Lithium (Al-Li) cryogenic tank [15]	48
3.13	Example of composite-fibre cryogenic tank from NASA [16]	51
3.14	Example of subscale composite-fibre cryogenic tank [17]	51
3.15	Examples of thermal protection system configurations for cyogenic tanks [14]	54
3.16	TPS concepts for nosecone and leading edges [14]	56
3.17	TPS concepts for upper edges, thermal insulation and cryogenic insulation [14]	57
4.1	Generic cylindrical shell structure and its reference system (α, β, z) , akin to those that will be used in the analyses [19]	62
4.2	A schematic description of the CUF and the related fundamental nucleus of the stiffness matrix for 3D, 2D and 1D models [19]	63
4.3	Employed approximations of the 1D (a) and 2D (b) models of a reference shell structure [26]	70
4.4	Different representations of the constraint equation located in Eq. 4.26 [24]	73

5.1	Beam geometry, cross-sectional mesh and representation of the load	77
5.2	Equilibrium curves of a cantilever square beam for different nonlinear approximations of a beam with aspect ratio $\frac{L}{h} = 10$	78
5.3	Von Mises stresses and deformed shape of the beam (fully nonlinear solution)	78
5.4	Beam geometry, cross-sectional mesh and representation of the loads	79
5.5	Post-buckling equilibrium curves for a thick ($\frac{L}{h} = 10$, Fig. 5.5a) and slender ($\frac{L}{h} = 100$, Fig. 5.5b) cantilever square beam	80
5.6	Deformed shape of the first four natural frequencies	82
5.7	Equilibrium curve of a shell for a fully nonlinear solution (the displacement is evaluated at the center of the structure); 10x10Q9 mesh, 1B3 cross-section	83
5.8	Deformed shapes for three different equilibrium states	83
5.9	Schematic diagram of the thin-walled semi cylindrical shell model with a concentrated load [23]	84
5.10	Convergence analysis of the model with a comparison between different in-plane meshes (5.10a, [23]); nonlinear equilibrium curve of the model using a 16x16Q9+1LD2 mesh compared with the results in [31] (5.10b, [23])	85
5.11	The initial undeformed structure and three deformed configurations of the semi cylindrical shell model for three equilibrium states [23]	86

List of Tables

2.1	Empirical expressions for knockdown factor calculation	16
2.2	Maximum steady-state acceleration for various launch vehicles [7] .	24
2.3	Example of sinusoidal vibrations [7]	25
2.4	Ranges of random vibrations [7]	25
2.5	Payload adapter induced shock at the spacecraft separation plane [8]	27
3.1	Comparison of mechanical properties between AF(UDRI) alloy and Al-Li 2195 alloy [14]	48
5.1	Convergence analysis of u_z for three different meshes	76
5.2	First ten natural frequencies (10x10Q9 mesh, 1B3 cross-section) . .	81

Abstract

Within the space transportation context, a new and exciting trend is emerging: the will of partially or fully reusing a launch vehicle. This allows LV manufacturers to offer more competitive prices in the overall growing space transportation market and further flexibility to customers. Many attempts at this have been done during the decades by governmental entities, approaching the problem in distinct ways: from horizontal takeoff-horizontal landing systems (HTHL, akin to an airplane) to vertical takeoff-vertical landing (VTVL) rockets by means of retropropulsion as in the case of SpaceX and Blue Origin, recently created privately owned space companies. This revolution in the business comes with necessary advancements in different aerospace fields, and the need of increasing the technology readiness level (TRL) of these technologies by means of research arises. Structural and thermal design problems that emerge with the will of reusability of launch vehicles are approached and preliminary considerations and proposals for solutions are reported and evaluated.

Introduction

Both manned and unmanned missions into space have been possible in the last, more or less, 70 years thanks to advancements in rocket technology. From the first intercontinental ballistic missiles refurbished for spaceflight, to the most modern and reliable launch vehicles of today.

Of course, in order to launch one of these vehicles and turn a bigger profit, launch vehicle designers have tried multiple solutions to reduce the weight of the launch vehicle itself, in order to be able to house heavier payloads while proposing lower launch costs for satellite manufacturers and, therefore, the clients that requested the spacecrafts in the first place.

In recent years, private space companies like SpaceX and Blue Origin have successfully design, tested and are operating LVs with parital or total reusability of the parts. By doing this, they have been able to drastically reduce the launch cost: for example, SpaceX's Falcon 9 and Falcon Heavy are capable of landing the used first stage of the rocket, maintain it and reuse it in a future launch. More information on the history of launch vehicles and why total or partial reusability is convenient can be found in Chapter 1.

Moreover, nowadays, in the name of reducing launch vehicle overall dry weight,

thin-walled shell structures are employed for the majority of the primary structures of the LV. These types of structures strongly reduce the required weight of the vehicle while maximising its load carrying capability. The key design considerations for these structures are reported in Chapter 2.

Lastly, in Chapter 3, the key problems afflicting the structural design of Reusable Launch Vehicles (RLVs) will be reported and analysed. Among the most glaring problems that the designer encounters there is the difficulty in the choice of adequate materials for thermal protection systems (TPS) for RLVs, cryogenic tank material choice and design, and cryoinsulation for the fuel tanks themselves.

Lastly, in Chapter 4 and Chapter 5, a theoretical introduction to the Carrera Unified Formulation is given. The formulation is specified in the case of geometrical nonlinearities. Examples of simple 1D and 2D structural models, with related nonlinear analyses, are reported; these were included in order to showcase the accuracy and efficiency of the CUF implemented into the *MUL*² software, capable of studying the nonlinear behaviour of thin-walled structures as encountered in cryogenic tanks and primary structures in reusable launch vehicles.

Final remarks, conclusions and future improvements will be drawn from the preliminary considerations that have been observed, and are reported in Chapter 6.

Chapter 1

Launch Vehicles and the Chances for Reusability

In the context of spaceflight, Launch Vehicles, or LVs, have had a vibrant and rich history in the past 70 years. From the space race during the Cold War to the most modern and ambitious projects of today, working to achieve the quest of manned interplanetary travel in order to make humanity interplanetary.

The *Enciclopedia Britannica* defines a LV as "a rocket-powered vehicle used to transport a spacecraft beyond Earth's atmosphere, either into orbit around Earth or to some other destination in outer space". [1] Crewed, Uncrewed mission and artificial satellites have used these kind of space vehicles since the 1950s.

In the beginning, the first LVs were essentially repurposed ballistic missiles developed for military applications throughout World War II. The design of the first vehicles made for space was pioneered by the likes of K. Tsiolkovkij in the USSR, R. Goddard in the US and H. Oberth in Germany. For instance, Tsiolkovkij was the first to recognize that a rocket with multiple stages was necessary in order to achieve orbital velocity needed while Goddard was the first to develop experimental

liquid fueled rockets.

During the Cold War, the US developed the first intercontinental ballistic missiles (ICMBs) to carry nuclear weapons transoceanically. Thanks to the leadership of Werner von Braun, these missiles were repurposed to launch the first US satellites and the first US astronaut, Alan Shepard. One of the ICBMs, the Atlas rocket was later used in the Gemini program in the mid-1960s.



Figure 1.1: Launch of the Saturn V during the Apollo 11 mission

During the 60s, NASA set out to design a LV capable of carrying humans to the moon and back. The Braun team successfully developed the Saturn V rocket, the world's most powerful rocket (until the successful launch of SpaceX Falcon Heavy). Thanks to this rocket, the notorious Apollo missions were carried out from 1968 to 1972, and this same rocket was used to launch and build the Skylab Space Station in 1973.

After the Apollo missions, the Saturn was retired from service in 1975, switching the American focus to the Space Shuttle, one of the first successful reusable spacecraft.

The Soviet story of launch vehicles begins very similarly to the US one. Under the leadership of S. Korolyov, in the 50s the USSR developed an ICBM able to carry nuclear warheads to the US. Soviet warheads were heavier than their American counterparts and this, in turn, meant that Soviet ICBMs were designed to have greater weight lifting capabilities than US ICBMs. This meant that, when used in spaceflight, the Soviet LVs had less problems using heavy payloads. The R-7 was used in order to send to orbit the first satellite ever, Sputnik 1, and the first Soviet cosmonaut and human to reach orbit, Yuri Gagarin.

A variant of the R-7 was the Soyuz, first used in 1966 and still active today (with subsequent improvements) and widely used for both manned and unmanned spaceflight.



Figure 1.2: A Soyuz rocket taking off from Baikonur Cosmodrome, KZ

Similarly to the US, in 1976 the Soviets began the development of the Buran space shuttle within the Energia launch vehicle program. The first launch of the Energia LV was reported in 1987 and the second in 1988, in which the Buran space shuttle was launched (with no crew). The program ultimately was discontinued due to high costs of launch.

Even if "a little late to the party", several European countries, led by France, decided it was time that Europe had its own space program, in order to be more independent from the US and USSR. In 1973 the European Space Agency (ESA) was formed and the Ariane heavy-lifting launch vehicle was being developed; the first Ariane launch was in 1979. This LV was not derived from previously available ICBM technology, differently from its peers. The development of the Ariane family led to the design and operation of the Ariane 5. The first launch was in 1996 and resulted in a failure; during its first rocky years successes and failures happened interchangeably, but since 2003 the Ariane 5 hasn't suffered any failures to date. Also in 2003, ESA decided to build a launch complex in Kourou, French Guiana, extending the medium-lifting capabilities and giving space access to manned missions through the Russian Soyuz LV. Ariane 6 is currently in development.



(a)



(b)

Figure 1.3: The Ariane 5 launch vehicle (Fig. 1.3a) and the Vega launch vehicle (Fig. 1.3b). *Courtesy of ESA*

The need for a smaller and more versatile European launch vehicle arose in the 2000s. This led to the development of Vega, whose first launch was in 2012. This LV allows a more affordable nano to micro satellite space access to the European SmallSat industry, and ESA itself. Further efforts and developments have been made

in recent years in this regard, thanks also to a redeveloped satellite dispenser for Vega, the Small Satellite Mission Service (SSMS), allowing for bigger ride-sharing capabilities on the LV.

1.1 Reusable Launch Vehicles

Launching payloads and reaching orbit with these LVs is, obviously very costly. This is a strong limiting factor, both for launch operators and for the global spacecraft industries. Since the start of the space age, there is been strong intentions in reducing these launch costs; the full or partial reusability of launchers is key in reducing launch costs.

Many attempts have been made throughout the decades, most notably the NASA X-33 project, a fully reusable single-stage-to-orbit LV that aspired of reaching suborbital heights without losing any parts, and returning to Earth for future reuse; the required materials and propulsion technology hadn't yet reached the maturity needed to bring this project into fruition.



(a)



(b)

Figure 1.4: The Space Shuttle (Fig. 1.4a) and the X-33 concept (Fig. 1.4b)

The aforementioned Space Shuttle program was a step in the right direction, even if the LV was only partially reusable. It was found out that, due to the high maintenance required and all the expendable parts on every launch, the single launch cost of the Space Shuttle exceeded the one of an expendable, traditional rocket. This is one of the reasons why the Space Shuttle program was discontinued. In recent years, more and more programs that aim to solve the reusability cost problem have emerged. More and more private space companies are working in order to develop cost-effective launch vehicles, both partially reusable or totally reusable.

As far as partially reusable LVs go, Vertical Takeoff-Vertical Landing (VTVL) launch systems have been tested, developed and are currently in operation; most notably the Falcon series from Space Exploration Technologies (SpaceX). In the early 2010s, SpaceX began work on developing a system that allowed the first stage of their Falcon 9 rocket to autonomously land, both on the launchpad and on a dronship in the middle on the ocean. They managed to land their first Falcon 9 first stage in December 2015. Since then, more and more first stages have been recovered, refurbished and reused in future flight, allowing the price of a single launch to be significantly lower than the competitors¹. A further development of this technology was applied for the Falcon Heavy, a heavy-lifting LV in which three first stages, essentially similar to the Falcon 9 ones, could be recovered in a single launch. Efforts at SpaceX are being made to increase parts reusability, as efforts to also recover the fairing thanks to nets mounted on boats are currently being made.

Another prevailing private space industry is Blue Origin, mainly founded by Jeff Bezos, the owner of Amazon. Blue Origin developed a fully reusable VTVL suborbital launch vehicle for space tourism purposes called New Shepard. Its first successful flight dates back to 2015, in which a soft landing was performed after reaching 100 km in altitude (the Karman Line) and is still in operation. Similarly to SpaceX, since 2012 Blue Origin has been developing an heavy-lifting LV with a reusable first stage, called the New Glenn, which aims at significantly reducing launch costs while increasing access capabilities to space. A first stage is rated for a minimum of 25 launches; New Glenn's first flight is scheduled to occur in 2021².

¹As reported on <http://cnb.cx/3ruUCpY>

²This and more information can be found at <https://www.blueorigin.com/new-glenn/>



(a) Falcon 9 first stage landing



(b) Falcon Heavy

Figure 1.5: The SpaceX family of reusable Launch Vehicles



(a) New Shepard



(b) New Glenn concept

Figure 1.6: The Blue Origin family of reusable Launch Vehicles

Chapter 2

Design of Thin-Walled Shell Space Structures

In this chapter, thin-walled structures will be discussed, as these are the most adopted type of structures in aerospace structural design.

In fact, thin-walled shells are widely used in launch vehicles due to their high load carrying capabilities and low weight. Tanks, interstage sections and payload adapters are made up of either cylindrical or conical thin-walled shells.

These key structural components are subjected to axial compression, both due to the weight of the above components exerted on them or the loads during launch.

After a general introduction on the most predominant problems affecting these structures and the most important design considerations, a section that will be dedicated to launch loads (in order to better understand the reasoning behind certain design choices) will be included for completeness. In between these two parts, the most interesting results (for this thesis work) from a NASA testing campaign on exactly these types of structures will be reported.

2.1 Introduction

As mentioned above, thin-walled shells are subjected mainly to compressive axial loads. This tends to make these structures buckle under those loads.

Buckling is a critical condition for shells; large deformations occur in the shell surface which is perpendicular to the loading direction. Buckling forms a pattern which propagates across a large portion of the shell's surfaces, causing a significant loss in the load carrying capability, which is the main strength on these structural elements. [2]

This means that buckling phenomena are one of the main drivers in the design of LVs thin-walled structures. Two examples of cylindrical shell buckling occurring under compressive loads are shown in Fig. 2.1.

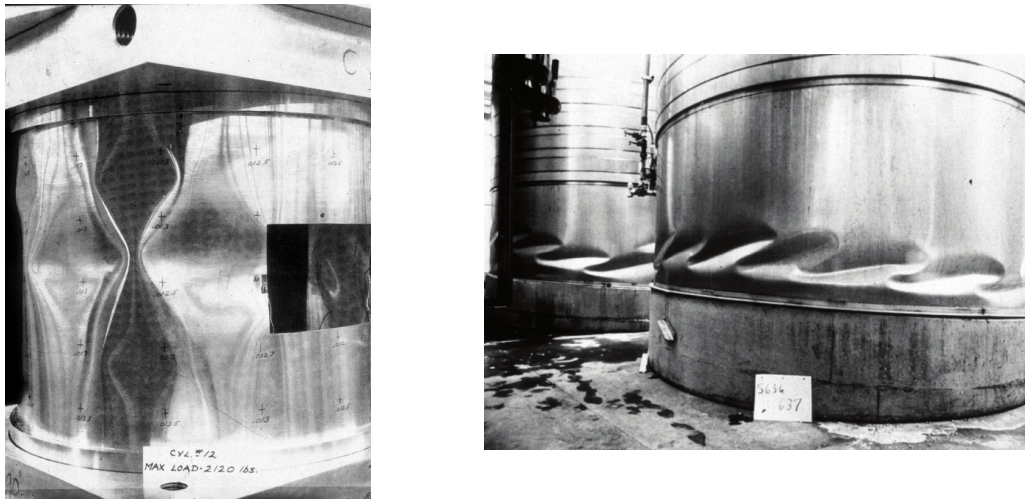


Figure 2.1: Examples of shells buckling under compressive loads

One of the main interests of buckling studies is to predict the maximum load carrying capability of launch vehicle thin-walled structures. This is further complicated by imperfections, as these types of structures are very sensitive to them. Geometric imperfections deviate from the theoretical estimation of the load carrying capability, as the ideal shape of the shell is different, reducing significantly the most important aspect of LVs shells.

Even today, guidelines for the design on cylindrical shells subjected to axial compression date back to recommendations from the 1960s, and studies have shown

how the resulting design factors are too conservative for modern LVs shells. One of the most important design recommendations reports by NASA used even today is ”*Buckling of thin-walled truncated shells*”. [3]

2.1.1 General Design Considerations

Considering a perfect, isotropic cylindrical shell, a relation for the buckling load has been derived in the literature, as

$$N_{per} = \frac{2\pi Et^2}{\sqrt{3(1-\nu^2)}} \quad (2.1)$$

where E is the elastic modulus, ν is the Poisson’s Ratio and t the wall thickness. Eq. 2.1 refers to shells in the prebuckling range with just a pure membrane stress rate. As it can be seen, it is independent from shell geometric variable like the cylinder radius or length. This equation leads to an inaccurate estimation of buckling load, especially compared to experimental results. This is due to the innate imperfection sensitivity of thin-walled shell structures subjected to axial compression.

Because of this, extensive testing campaigns in the 20th century lead to the formulation of a *knockdown factor* (KDF) ρ (graphically represented in Fig. 2.2), which is simply the ration between experimental calculated buckling load and the theoretical buckling load derived from 2.1:

$$\rho_{exp} = \frac{N_{exp}}{N_{per}} \quad (2.2)$$

As previously mentioned, geometrical imperfections are the main cause in the reduction of the buckling load for these particular structures. Studies have shown how the buckling load for isotropic cylinders is very sensitive to both the nature of the initial geometric imperfection and shell geometry (R/t and L/R), therefore a precise assessment of these imperfections is imperative when designing cylindrical shells.

To do this, one approach could be to measure these imperfections directly on components already built for testing porpouses, in order to subsequently implement the observed imperfections in, for example, a finite element model for future use.

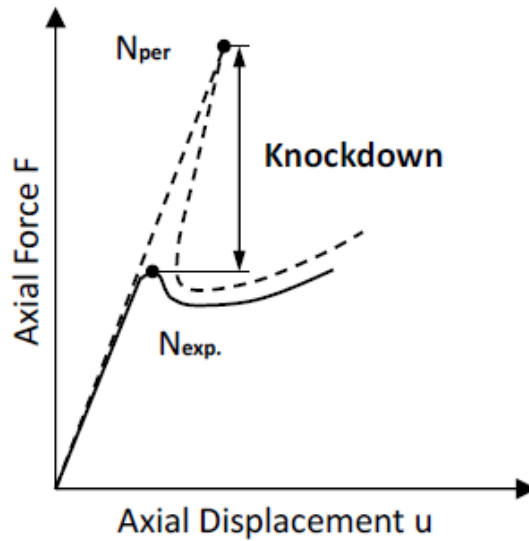


Figure 2.2: The knockdown factor on the load-displacement curve [2]

This approach requires a lot of time and is expensive, and the studies cannot be executed on all types of cylindrical shell structures, therefore these may not be able to be applied on large-scale structures, which is the main interest.

Another approach is to "stimulate" a characteristic physical buckling response (fabricated by shape deviations, like axial welds or cutouts in the structure). This was the main concept adopted in NASA's Shell Buckling Knockdown Factors (SBKF) project [4], in which it was shown how weld land buckling is the most dominant with respect to, for example, geometric imperfections.

Studies about dimple deformations in cylindrical shells due to axial compression were performed since the 1970s. It was observed that, adding an external perturbation (a lateral force), the corresponding buckling load was in the range of 35 to 50% that of the one calculated with Eq. 2.1. [5]

A load above 50% of this classical buckling load leads to global buckling of the shell. The corresponding compressive load is called *Global buckling load*; in addition, a local snap in the surface of the cylinder can be observed (it creates a diamond-shaped dimple in the surface). The associated compressive load for this phenomena is called *Local buckling load*. Both of these critical buckling loads have been further examined and studied in [6]. These results can be better understood in Fig. 2.3.

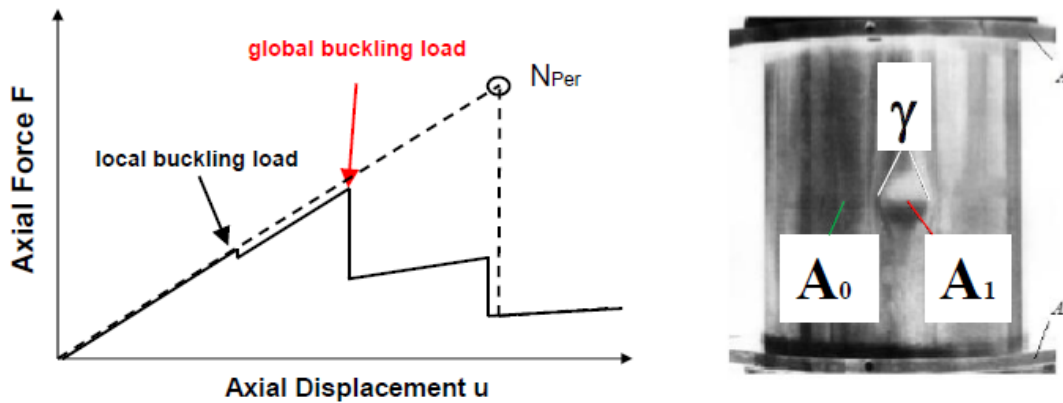


Figure 2.3: Global and local buckling loads (unstiffened cylinder, right), diamond-shaped dimple (left) [2]

Further studies presented evidence to how, for small external applied loads applied to halfway the length of the cylinder, the buckling load tends to be close to the one calculated considering a perfect cylinder (N_{per}). Increasing this perturbation leads to a reduction of the buckling load N but, after a certain point, the buckling load is essentially constant even if the perturbation load increases.

The resulting buckling load between sections 2 and 3 in Fig. 2.4 is defined as the *design load* N_{SPLA} . This methodology is therefore called the Single Perturbation Load Approach (SPLA) and is widely used to this day.

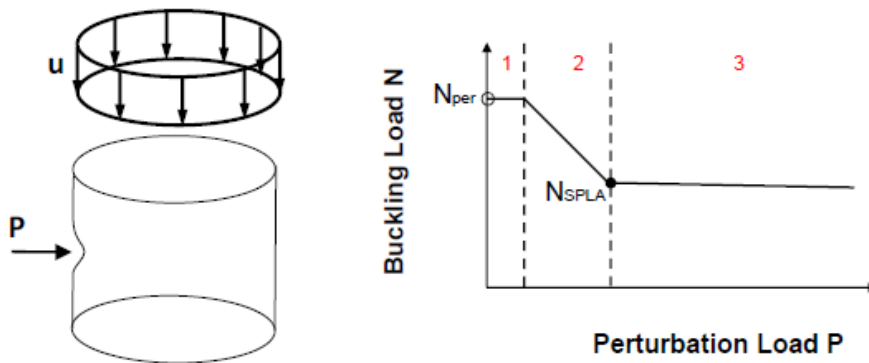


Figure 2.4: The Single Perturbation Load Approach diagram [2]

Coming back to the discussion regarding knockdown factors, over the decades, various publications found different empirical expressions in order to calculate them.

These expressions represent the lower-boundary curves based on experimental research and reliability levels; the most relevant are reported in Table 2.1 and Fig. 2.5.

KDF formulation ($N_{des} = \rho \cdot N_{per}$)		Year
$\rho = 14.9 \left(\frac{t}{R}\right)^{0.6}$	Kanemitsu and Nojima	1939
$\rho = 6.35 \left(\frac{t}{R}\right)^{0.54}$	Gerard and Becker	1957
$\rho = 1 - 0.902 (1 - e)^{-\left(\frac{1}{16}\sqrt{\frac{R}{t}}\right)}$	NASA SP-8007	1965
$\rho = 3.87 \left(\frac{R}{t}\right)^{-0.5}$	Russian guidelines	1978
$\rho = \frac{0.7}{\sqrt{1 + \left(\frac{1}{100}\frac{R}{t}\right)}}$	German guidelines	1980

Table 2.1: Empirical expressions for knockdown factor calculation

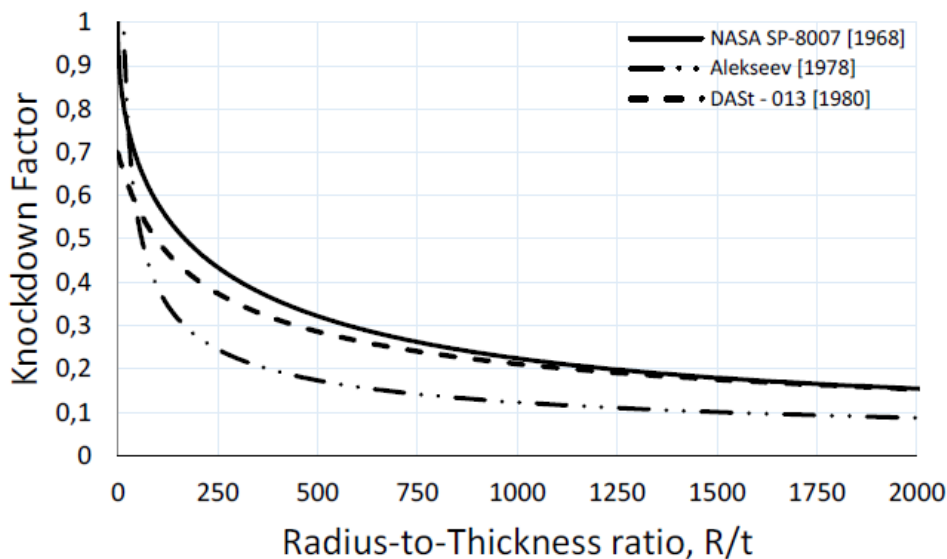


Figure 2.5: Empirical KDFs lower-boundary curves for cylindrical shells as a function of R/t [2]

2.2 Stiffening Techniques and NASA Testing Campaign

In the following section, the most adopted stiffening techniques used in order to increase the load carrying capability of thin-walled shells will be presented. Subsequently, the most interesting results, and how the efficacy of these techniques was evaluated in NASA's SBKF project.

As reported in [4], throughout NASA's Shell Buckling Knockdown Factor (SBKF) project a comprehensive test program to investigate the buckling response of integrally stiffened metallic cylinders was completed. This testing campaign included an analysis of eight small scale 8 ft diameter cylinders and two full scale 27.5 ft diameter cylinders.

Various loading conditions were applied to the cylinders and include different combinations of axial compression, bending, and internal pressure loads that simulate typical LV loads. The data gathered from the program is currently being used to develop and validate new knockdown factors and design guidelines for these stiffened cylinders by analysis.

Each test article was constructed from three fully stiffened, 2195 Al-Li curved-panel segments (120° arc segments) that were welded together to form a complete thin-walled cylinder. The chosen stiffener configurations were an internal orthogrid stiffener pattern (Fig. 2.6a) and an isogrid stiffener pattern (Fig. 2.6b).

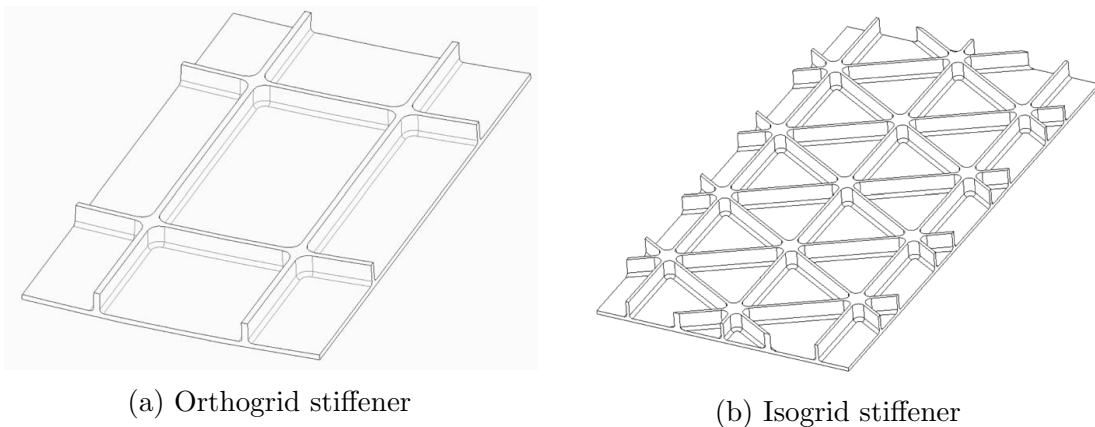


Figure 2.6: Stiffening techniques used in [4]

In order to determine the corresponding cylinder-radius-to-effective-thickness ratio R/t_{eff} the following equation was used:

$$t_{eff} = \sqrt[4]{\frac{144D_{11}D_{22}}{A_{11}A_{22}}} \quad (2.3)$$

where $D_{11}D_{22}$ are the bending stiffnesses in the axial and the circumferential directions, respectively, and $A_{11}A_{22}$ are the membrane stiffnesses in the axial and the circumferential directions, respectively.

R/t_{eff} values range from 80.1 to 230.9 and cover a significant portion of the relevant launch vehicle design.

2.2.1 Results for Orthogrid Stiffened Shell

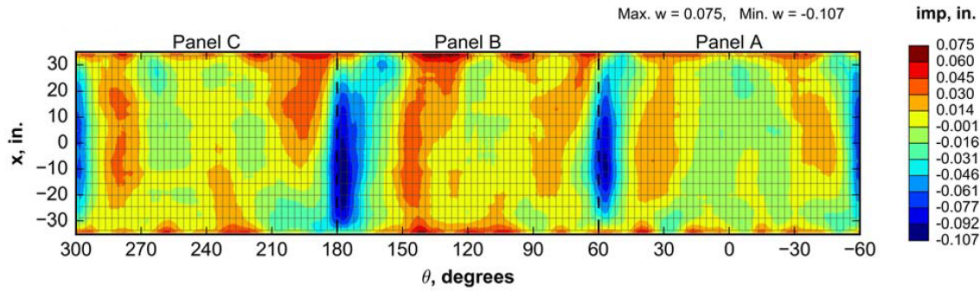


Figure 2.7: Measured geometric imperfections in inches (blue and red contours correspond to inward and outward radial imperfections, respectively)

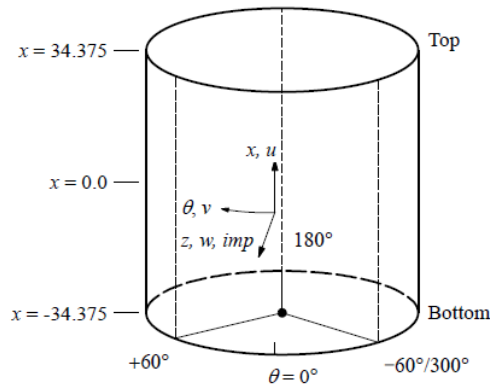


Figure 2.8: Cylindrical Coordinate System

A typical measured geometric imperfection from the manufactured cylinder is shown in Fig. 2.7 and corresponds to the difference between the measured constructed geometry and an ideal circular cylinder. The coordinate system used to display this imperfection data is defined in Fig. 2.8. Per this coordinate system, the location of panel A is between -60° and $+60^\circ$, panel B is between $+60^\circ$ and 180° , and panel C is between 180° and -60° . The weld points were named after the panels they join: A/B, B/C and C/A. The blue and red colored contours in Figure 2.7 correspond to inward and outward radial imperfections, respectively. The measured imperfection exhibits distinct inward imperfections at the three axial weld points, at $\theta = -60^\circ$, 60° , and 180° , of approximately -0.10 inches and smaller magnitude variations in the acreage of the cylinder. This measured imperfection shape and amplitude were found to be typical for the 8 ft diameter cylinders tested and share many common features as those seen in full-scale welded cylinders. [4]

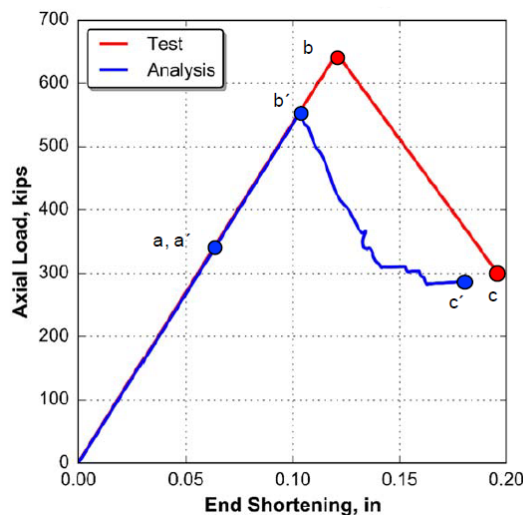


Figure 2.9: Predicted and measured load versus end-shortening response curves

Predicted and measured axial load against end shortening response curves are shown in Fig. 2.9. The test article exhibited a linear response up a maximum load of 647.0 kips (2.88 MN) at which point, buckling initiated and the cylinder collapsed. Upon buckling and collapse, the cylinder experienced a 51.7% reduction in axial load to a relatively stable postbuckling load level of 312.2 kips (1.39 MN). During the collapse, the test article underwent a rapid increase in end-shortening from 0.12 inches to

0.19 inches, and is attributed to the unloading response of the load introduction structure that imparted a sudden additional end-shortening displacement onto the test article. The predicted load-end-shortening curve indicated a similar linear prebuckling response, but achieves a buckling load of 554 kips (2.46 MN), 14.4% less than the measured result. In addition, the predicted results indicated a similar increase in end-shortening during the transient collapse event. [4]

Measured prebuckling, incipient buckling, and post-buckling radial displacement contours are shown in Fig. 2.10 and correspond to points **a**, **b**, and **c** on the load end-shortening plot in Fig. 2.9. The prebuckling deformations, shown in Fig. 2.10a, are characterized by local inward radial displacements along each of the three weld lands, and alternating regions of inward and outward radial displacements within each of the panel segments. As the cylinder approached the buckling load at point **b**, the inward radial displacements in the B/C weld land begin to localize into a single dimple near the bottom attachment ring, as shown in Fig. 2.10b. Upon buckling, additional buckles formed around the entire circumference of the cylinder, resulting in the overall collapse of the structure, shown in Fig. 2.10c, and corresponding to point **c** in Fig. 2.9. [4]

Predicted prebuckling, incipient buckling, and initial post-buckling displacement contours are presented in Fig. 2.11 correspond to points **a'**, **b'**, and **c'** in Fig. 2.9. The displacement contours exhibit similar characteristics as the measured contours shown in Fig. 2.10. In particular, the prebuckling response is characterized by local inward radial displacements along each of the three weld lands, and alternating regions of inward and outward radial displacements within each of the panel segments as shown in Fig. 2.11a. As the cylinder approached the buckling load, inward radial displacements began to localize into a single dimple near the bottom of the cylinder in the A/B weld land, as shown in Fig. 2.11b. Upon, buckling, additional buckles formed around the entire circumference of the cylinder, corresponding to the overall collapse of the structure as shown in Fig. 2.11c, corresponding to point **c'** in Fig. 2.9. [4]

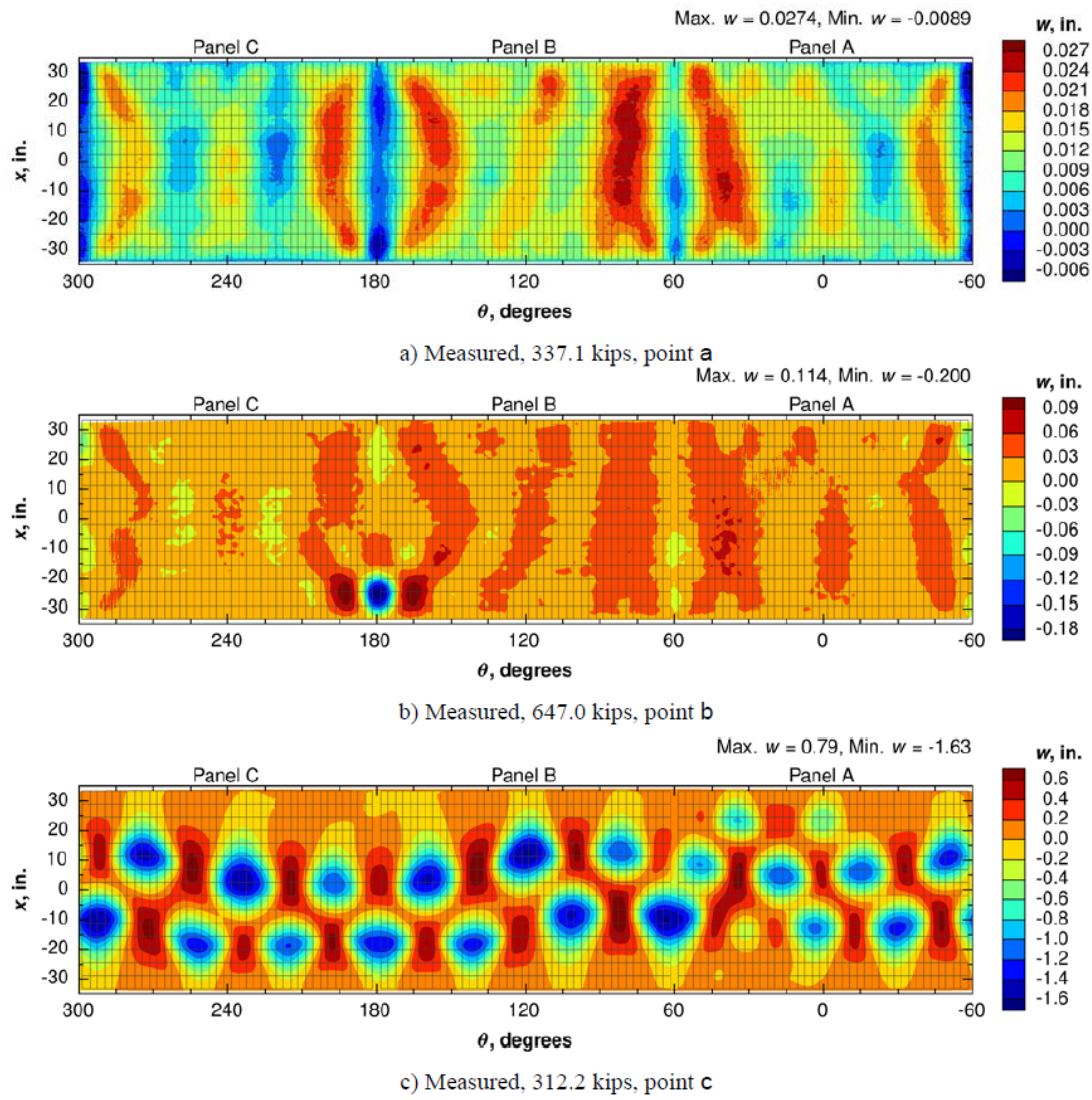


Figure 2.10: Measured prebuckling (point a), incipient buckling (point b), and postbuckling (point c) radial displacements

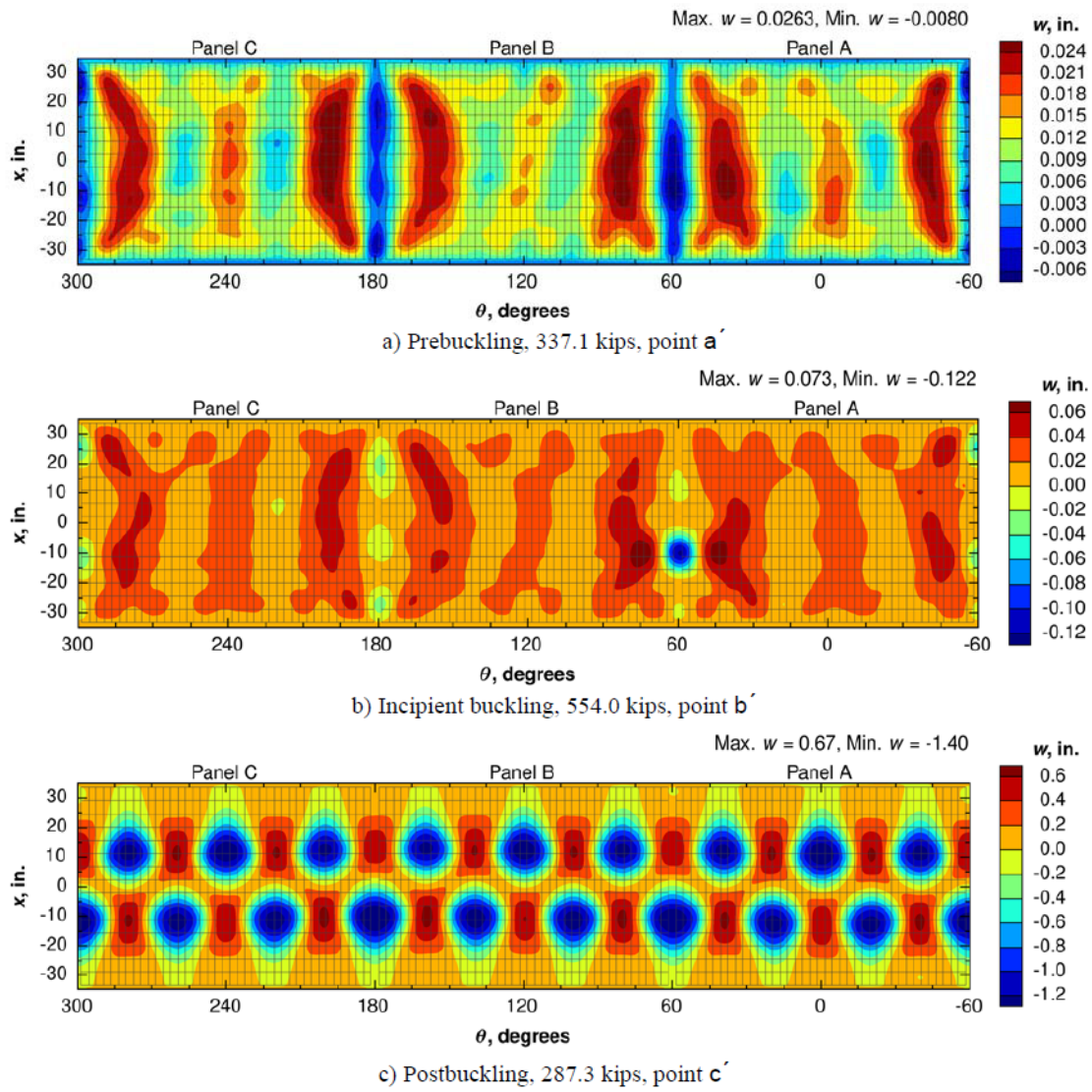


Figure 2.11: Predicted prebuckling, incipient buckling, and postbuckling radial displacements

2.3 Launch Loads

In this last section, the main loads to which a launch vehicle is subjected to during launch will be briefly explained. All the different launch loads are reported to costumers in the LV's respective User Manuals, as different loads are expected for different launchers. Customers that are willing to use the services of a particular LV must certify that their payload is compliant and able to sustain the reported loads. During the ascent profile, an LV encounters low frequency loads, mainly caused by transients, like engine ignition or shutdown, wind shears and quasi-static loads. Other environments are acoustics, random and sine vibrations, and shock loads. [7] The maximum loads are used in order to design and dimension the primary and secondary structural components.

Transportation Loads

The first type of loads that a spacecraft encounters are transportation loads. These loads are caused by the fact that components and payloads need to be transported to the launch site at some point in time, and these need to be taken into account in the design process. These loads vary with respect to the medium used to transport the spacecraft: for example, maximum loads of about ± 2.5 g are to be expected if travelling at sea, and up to ± 6 g when transported by truck.

Steady-State Loads

The steady-state maximum acceleration occurs at the end of the propulsion phase, as the overall mass of the LV decreases (as fuel is consumed) while maintaining the same thrust levels. The maximum accelerations are mainly in the longitudinal direction, as lateral one are usually negligible.

For completeness, some examples of the maximum steady-state acceleration for different LVs is reported in Table 2.2, and an example of the accepted axial and lateral accelerations envelope throughout the launch for the SpaceX Falcon family of launchers is presented in Fig. 2.12. This envelope comes directly from the Falcon User's Guide [8].

Launch Vehicle	Maximum Steady-State Acceleration	
	Longitudinal [g]	Lateral [g]
Ariane 4	4.5	0.2
Ariane 5	4.25	0.2
Atlas	5.5	0.4
Proton	4	0
Falcon 9	6	0.5

Table 2.2: Maximum steady-state acceleration for various launch vehicles [7]

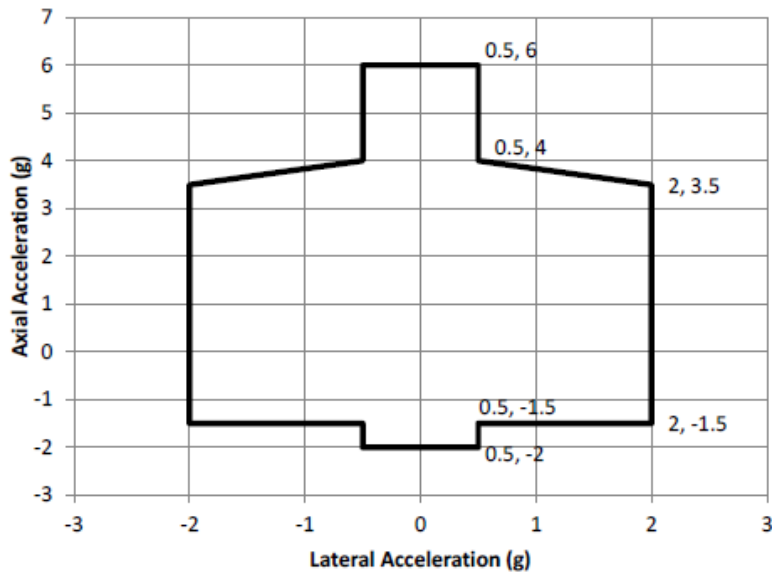


Figure 2.12: Falcon 9 and Falcon Heavy payload design load factors [8]

Dynamic Loads

During launch there are essentially two types of mechanical dynamic loads. The first are low frequency sinusoidal vibrations (range 5-100 Hz) and second one are random vibrations (low to high frequency, range 20-2000 Hz).

The first type appears as there is an interaction between characteristic mode shapes and loads that occur during lift off and during engine combustion. In Table 2.3, examples of usual values of sinusoidal vibrations are reported.

	Frequency [Hz]	Acceleration [g]
Launch direction	5-6.2	12.7 mm double amplitude
	6.2-100	1.0
Lateral direction	5-100	0.7

Table 2.3: Example of sinusoidal vibrations [7]

Random Loads

During launch, turbulence on the LV and acoustic loads carry onto the launcher and turn into mechanical vibrations, also affecting the payload. Some ranges of random vibrations are given in Table 2.4.

Frequency Range [Hz]	PSD [g^2/Hz]	rms acceleration [g]
20-150	+6db/octave	
150-700	0.04	7.3
700-2000	-3db/octave	

Table 2.4: Ranges of random vibrations [7]

The rms, or root mean square, of a random signal $x(t)$ with a certain period T is

$$x_{rms} = \left[\lim_{T \rightarrow \infty} \frac{1}{T} \int_{-T/2}^{T/2} x^2(t) dt \right]^{0.5} \quad (2.4)$$

while the Power Spectral Density (PSD) function in the frequency domain is

$$W_{xx}(\omega) = 2S_{xx}(\omega) \quad (2.5)$$

The square root mean value $x(t)$ becomes

$$x_{rms} = \sqrt{\int_0^{\infty} W_{xx}(f) df} \quad (2.6)$$

For a more in depth evaluation the reader is referred to [7].

Acoustic Loads

Acoustic loads are generated during launch due to aerodynamic drag and flow separation. The aerodynamic noise therefore generates acoustic loads in the range of 20-10000 Hz. This loads translate into high frequency random vibrations, and it's at its peak during the maximum aerodynamic pressure phase (transonic flight). In Fig. 2.13an example of a specified acoustic load spectrum, taken from the Falcon's User Manual, is presented for completeness.

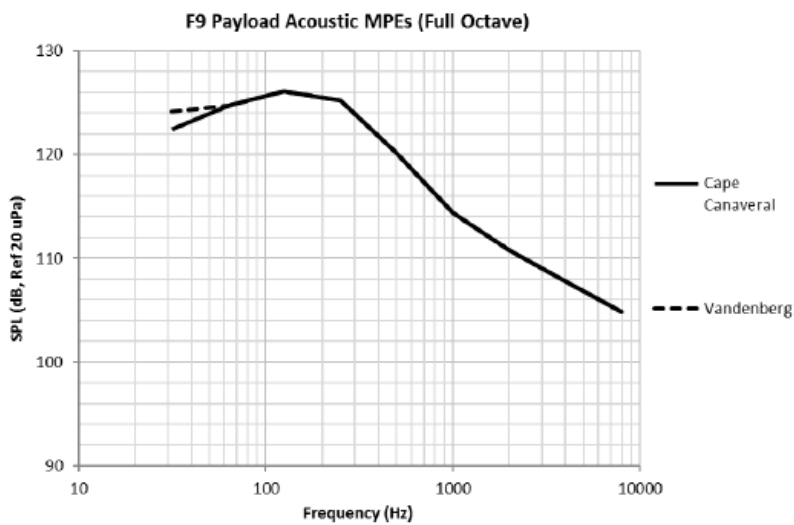


Figure 2.13: Example of Falcon 9 maximum predicted environment, both from Cape Canaveral and Vandenberg Base [8]

Shock Loads

Shock loads are very short duration loads that occur when the spacecraft or the stages separate during flight. The effects of these occurrences are normally represented in a Shock Response Spectrum (SRS), a plot that shows the responses of a number of single degree of freedom system to an excitation.

”The spacecraft is generally loaded by the heaviest loads when the nose cone is fired away and when the spacecraft separates from the last stage of the launch vehicle. The combustion and the burn-up of the engines generally result in lower shock loads.” [7]

An example of shock induced at the spacecraft separation plane in a Falcon 9 is reported in Table 2.5.

Frequency [Hz]	SRS [g]
100	30
1000	1000
10000	1000

Table 2.5: Payload adapter induced shock at the spacecraft separation plane [8]

Chapter 3

Key Problems in the Structural Design of RLVs

In this chapter, a further analysis of possible methodologies employed to reuse a launch vehicle are reported. A better subdivision between the most common landing systems will be done; to be specific, two systems will be further explained: the Vertical Takeoff-Vertical Landing (VTVL) reusable launch vehicles (RLVs), akin to the ones used for SpaceX Falcon family and Blue Origin New Shepard and New Glenn, and Vertical Takeoff-Horizontal Landing (VTHL) RLVs, like the Department of Defense X-33 prototype or NASA Space Shuttle.

For these types of reusable LVs, the most important problems and considerations regarding the structural design changes needed to utilise these LVs will be reported and finally some proposals and recommendations will be given to reduce launch risks of RLVs.

3.1 Types of Reusable Launch Vehicles

In recent decades, the Space Shuttle program has highlighted the strong impact that a reusable launch vehicle can have on the space industry, even if it has been found how the refurbishment costs for the maintenance of that RLV could not be contained appropriately and resulted in higher overall cost of the program. Nonetheless, the Space Shuttle has proven itself for its versatility and innovation in the space transportation business. The Space Shuttle is categorized as a Vertical Takeoff-Horizontal Landing system, as the vehicle initially takes off thanks to auxiliary, expendable solid rocket boosters and later lands on its own thanks to advanced heat shields and aerodynamic surfaces for reentry controllability (wings).

Recent times however have seen a shift in perspective regarding the RLV industry, more precisely considering vehicles that land vertically thanks to retropropulsion, like the Falcon family or the Blue Origin rockets. This opened up the concrete possibility of using this kind of technology in order to reduce launch service costs. Thanks to the possibility shown by SpaceX, foreign space agencies have begun to dabble with the idea of developing a reusable launcher of their own, in order to stay competitive in the evolving market and also to reduce launch costs and offer further flexibility to customers; one of these agencies is the European Space Agency (ESA).

Within this context, in 2017 the DLR project AKIRA was started. [9] [10]

One of its main purposes is to raise the technology readiness level (TRL) of key technologies for the use in reusable launch vehicles, like cryogenic insulation of tanks and innovative thermal protection systems.

When considering a new space reusable launch system, it's important to draw comparisons between different return options, in order to identify benefits and problems.

As previously mentioned, the main differences between Vertical Takeoff-Vertical Landing (VTVL) RLVs and Vertical Takeoff-Horizontal Landing (VTHL) RLVs will now be further detailed, together with their most important characteristics.

3.1.1 Vertical Takeoff-Vertical Landing RLVs

The first, and most commonly known nowadays, way of partially reusing a launch vehicle is the Vertical Takeoff-vertical Landing (VTVL) approach. It is generally known as the major privately owned space companies like SpaceX and Blue Origin have successfully developed, implemented and achieved partial reusability (or total reusability in the case of Blue Origin's New Shepard, even if the scope of this LV is smaller compared to the competition) of the rocket.

As previously mentioned, this method relies on retropropulsion as a means of landing vertically the first stage of a two-stage-to-orbit LV.

This is done by re-igniting the stage 1 engine after main engine cutoff (MECO) and successful separation of the first stage from the rest of the rocket. After this, there are essentially two options that have been tested and successfully carried out for reentry of the first stage: the first option relies on certain correction manoeuvres that allow the first stage to land near the initial launch site, while the second option relies on a barge (a dronship) positioned in the middle of the Atlantic Ocean (as the main launch site for both SpaceX and in the future Blue Origin is Cape Canaveral, Florida) in which the first stage is directed to in order to perform the landing.

The first way is called return to launch site (RTL) while the second one is called downrange landing (DRL). RTL requires additional fuel in order to reduce the horizontal velocity vector and invert the first stage to the launch site, while the second one requires, as already said, an additional infrastructure (the barge in open sea) and therefore better logistical coordination.

These manoeuvres are supported by additional components designed to control the reentry of the vehicle, like grid fins, and to land the first stage (landing legs).

The RTL method can be appreciated in Fig. 3.2, where a typical mission profile for a Falcon 9 is presented; similarly, in Fig. 3.1, a future typical mission profile for the New Glenn rocket can be appreciated.

An example of the DRL method is presented in Fig. 3.3, where a mission profile for the Falcon Heavy rocket (which lands three different first stages, two using the RTL method and one subsequently using the DRL method) is reported.

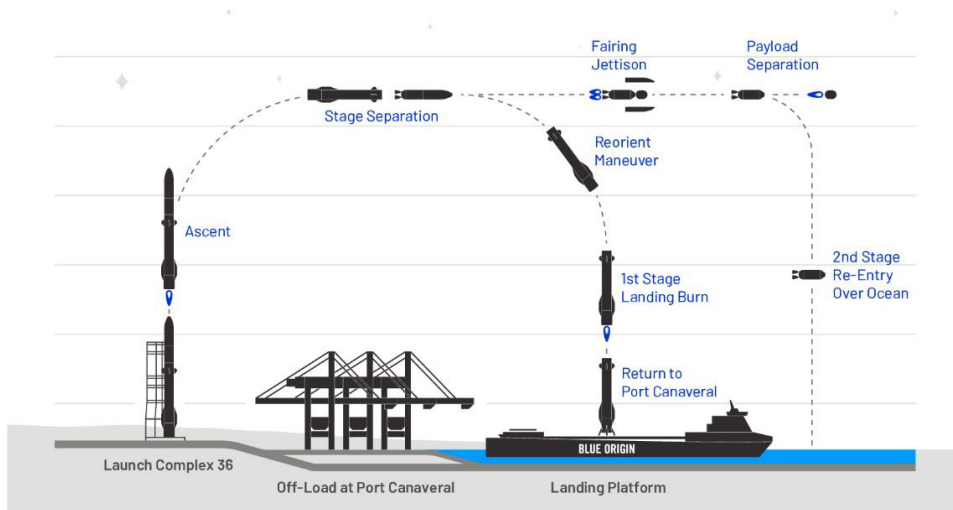


Figure 3.1: Typical mission profile for the future Blue Origin New Glenn rocket [11]

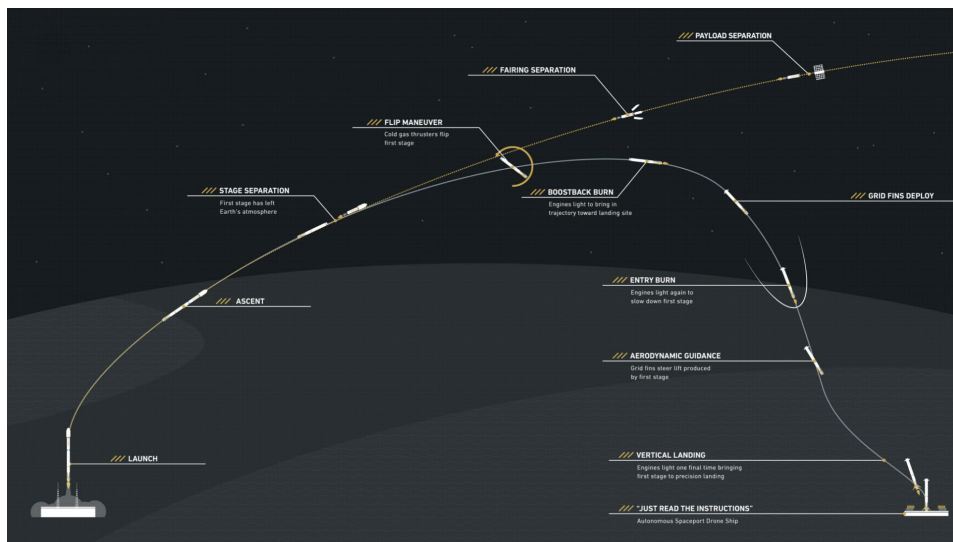


Figure 3.2: Typical mission profile for a SpaceX Falcon 9 rocket [8]

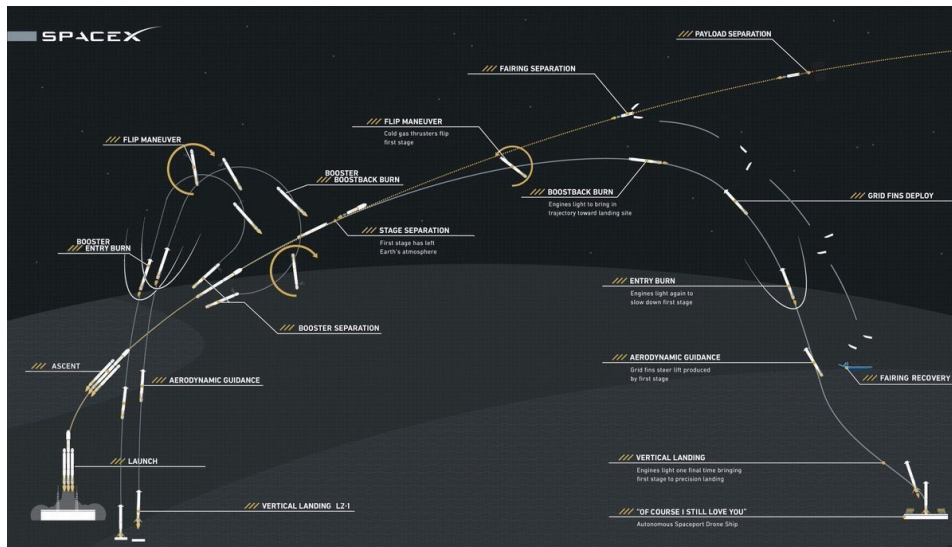


Figure 3.3: Typical mission profile for a SpaceX Falcon Heavy rocket [8]

When considering how the thin-walled structures are to be designed in a VTVL rocket, cryogenic insulation is to be considered in the case of liquid hydrogen used as fuel. This need no longer arises when considering hydrocarbon-based fuels like RP-1 (for example used in Falcon 9). The safety factor chosen for the design should be 1.25, a standard value for unmanned launch vehicles.

In the case of a two-stage-to-orbit LV using hydrocarbon-based fuels, the tanks and the second stage skirt can be designed with a conventional approach of using stringers and frames. The number and configuration can be chosen using computational optimization techniques. A standard space-graded aluminum can be used to build the components. The fairing and the interstage can be built using aluminum honeycomb structures reinforced with carbon fiber outer layers, while the reusable first stage's frame can be modelled with an elongated conical structure formed with stringers and frames.

A sketch of the structural model is reported in Fig. 3.4, where the green parts are the front and rear skirts and the blue parts represent the cylindrical thin-walled tanks.

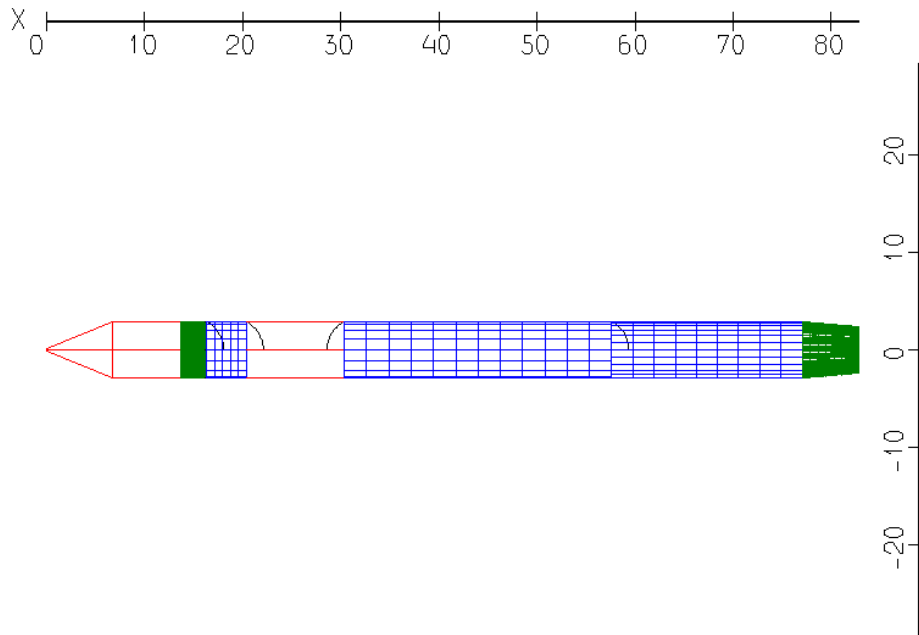


Figure 3.4: Structural model for a preliminary hydrogen RLV [12]

With regards to the operational procedures of recovering these types of reusable launch vehicles, a couple of different approaches have been proposed and one has been implemented since 2016.

The first method consists in landing the first stage on a unmanned droneship in the ocean. This method requires additional hardware, facilities and manpower; this ship has also less maneuverability. An alternative, proposed by Blue Origin for their upcoming LV with a reusable first stage, is using a repurposed larger, more agile, ship for the first stage landings.

In the method used at SpaceX, the droneships require a positioning system which stabilizes the ship at sea, systems to communicate with the descending stage, structural reinforcements of the pad and appropriate hardware to securely fix and transport the LV after landing. Once the stage has landed, two vessels in proximity carry on board the personnel needed to tug the droneship to shore. Furthermore, tugboats are required, and once the ship has reached shore, cranes and lifting devices are needed, in addition to specialized vehicles to carry the first stage to the refurbishment facilities. The main advantage of this method is the low acquisition cost and high flexibility; on the other hand, major disadvantages include a high travel time due

to the low speed of the tugboats and the need of a lot of vessels for the recovery operations.

The Blue Origin approach differs a bit from the SpaceX one with regards to down-range landing operations. They have in fact acquired a RoRo ship, which is a large ship more maneuverable than a simple tugboat. The first stage will land on the ship itself, on a modified pad. The ship itself will manoeuvre to shore, with no need for additional ship to assist the recovery operations. In this case the acquisition costs are higher but, due to the multipurpose design of the ship, the travel times are vastly reduced.

If the mission profile allows it, the return-to-launch-site approach is the best one available with regards to operational procedures. The stage autonomously returns to the launch site, with no need of additional infrastructures (the ships themselves or the hardware needed at the docks), greatly reducing costs and avoid travel times. Communication hardware and an available concrete pad are what would be needed in this case.

3.1.2 Vertical Takeoff-Horizontal Landing RLVs

The second way of landing and reusing a space vehicle is the Vertical Takeoff-Horizontal Landing (VTHL) approach; a very well known example is the NASA Space Shuttle program.

In opposition with the VTVL method, the VTHL approach consists in a deceleration of the launch vehicle by aerodynamic surfaces after the Main Engine Cutoff phase. The engine's thrust is not utilized. These kinds of vehicles feature aerodynamic control surfaces, like wings, in order to generate sufficient aerodynamic forces to land horizontally.

An additional method for landing VTHL launch vehicles, is the so called In-Air-Capturing, in which the returning first stage is captured in mid air by an airplane. This idea has been previously contemplated in the AKIRA project within the DLR. An example of an In-Air-Capturing mission profile is reported in Fig. 3.5.

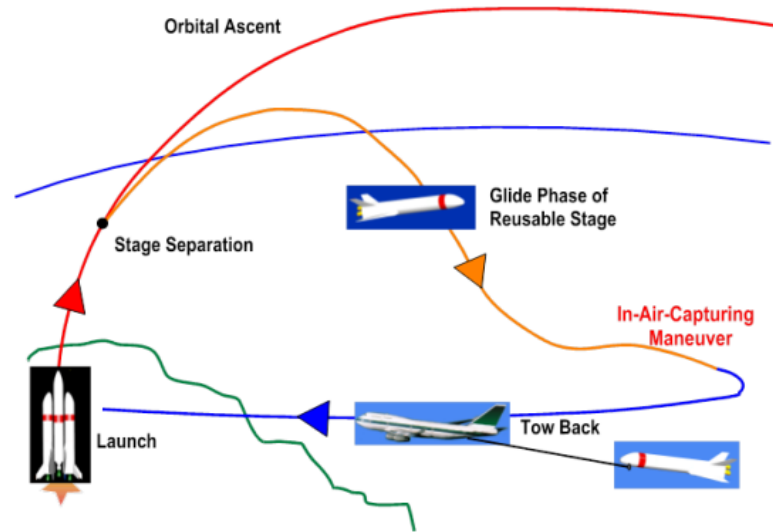


Figure 3.5: Sketch of a sample In-Air-Capturing mission profile [10]

Operational procedures for VTHL launch vehicles can be compared to VTVL ones. In fact, the landing is executed by means of an in-air-capturing, meaning that the returning stage is captured mid-air by an airplane and then towed back to a landing site, akin to a dronship in the ocean that carries the reusable stage back to shore. Therefore, an airborne vessel is needed for this reusability method.

In particular, several second hand vehicles can be selected to complete the task of catching and leading back the RLV to a landing strip; examples of these airplanes include the Boeing 747-400, Boeing 747-8F and the Airbus 340-400. For the B747 a large second hand market is available, and the price of these planes can vary with their age and condition (used Boeing 747s can be found for between 16 and 32 million dollars).

It also becomes necessary to include modifications to be applied to the craft (like structural reinforcements and the installation of the capturing system itself), and should be predisposed to be flown remotely for security purposes.

Some considerations for the post-landing phase are to be done: the first stage has to be depressurized and the remaining fuel and oxidizer have to be removed; these facilities are to be implemented in the chosen airport in which the aircraft will land. Furthermore, adequate airstrips and hangars are to be predisposed at the airport in

order to service the first stage and allow for the refurbishment.

3.1.3 Technological Comparisons

In [10], different conceptual designs of RLVs, both with VTVL and VTHL approaches, have been technologically compared. These are reported in Fig. 3.6.

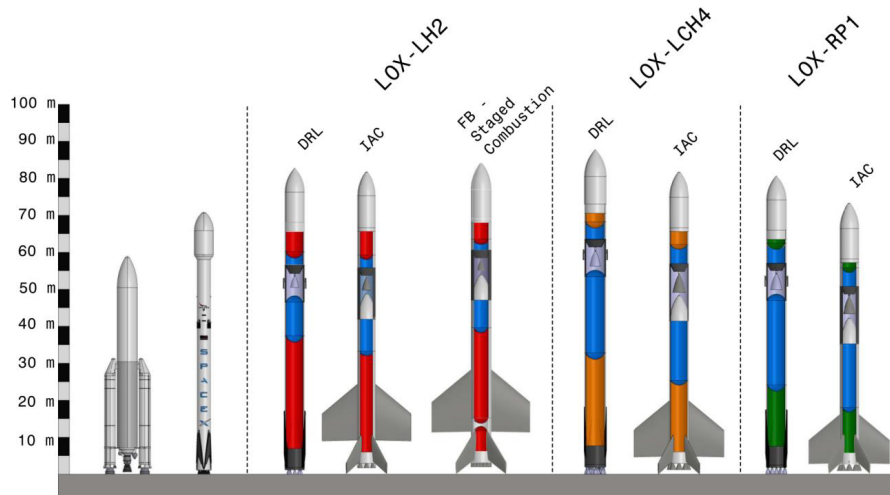


Figure 3.6: Size and architecture of some conceptual VTVL and VTHL RLVs compared to Falcon 9 and Ariane 5 [10]

In the research it was found that ”the LOX/LH2 launchers are smaller and lighter compared to the hydrocarbon launchers which are about 2.7 times heavier in case of VTVL, and around twice as heavy in case of VTHL (see Fig. 3.7). This came unexpected since the low density and high structural indices of the LOX/LH2 combination, although delivering a high specific impulse was expected to lead to bigger launchers. The reason for that is that the higher I_{sp} of the LOX/LH2 combination has two advantageous impacts on the launcher design. First, the higher I_{sp} in general requires less propellant mass. In case of the VTVLs, the higher I_{sp} further requires less propellant mass for the descent maneuvers, thus in turn leading to a lower inert mass that has to be accelerated during ascent. This also explains the greater mass increase when switching from hydrogen to hydrocarbons as fuel in case of the VTVLs.” [10]

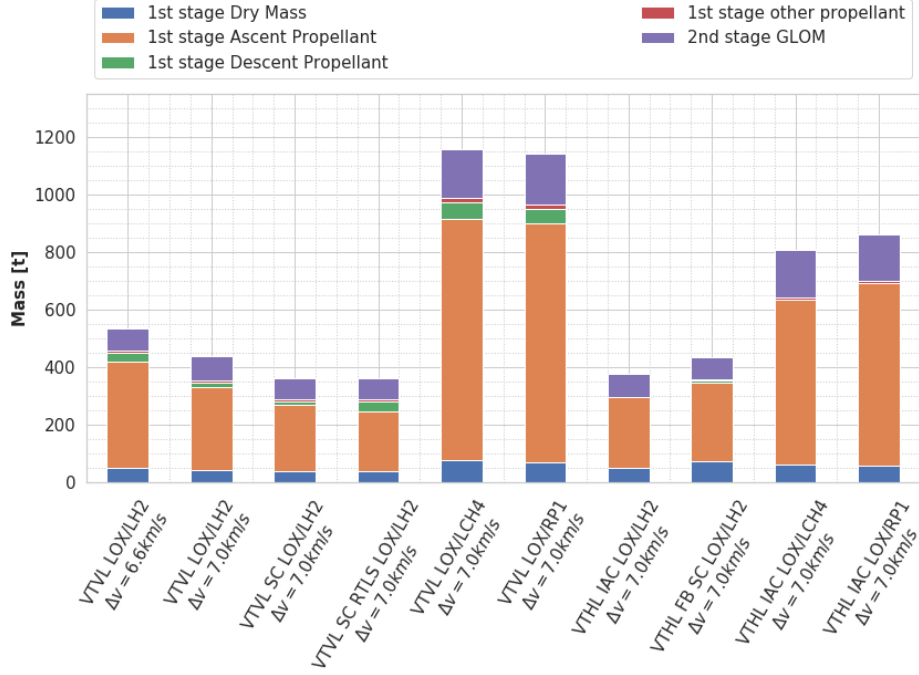


Figure 3.7: Mass comparison between the aforementioned conceptual RLVs [10]

It can be also observed how VTVL launch vehicles are bigger than winged vehicles; this can be simply explained as the former require more fuel (and therefore bigger and heavier tanks), while the latter has a mass increase only due to the presence of wings and aerodynamic surfaces.

In Fig. 3.8, a comparison between the different configurations is done by means of structural and inert mass indices.

The Structural Index is defined as

$$\text{Structural Index} = \frac{m_{dry}}{m_{prop}} \quad (3.1)$$

with m_{dry} being the dry mass of the reusable first stage and m_{prop} the total propellant mass of the first stage. Similarly, the Inert Mass Index is defined as

$$\text{Inert Mass Index} = \frac{m_{inert}}{m_{prop}} \quad (3.2)$$

as m_{inert} includes propellant mass needed for the descent phase, the dry mass, residuals and possible reserves.

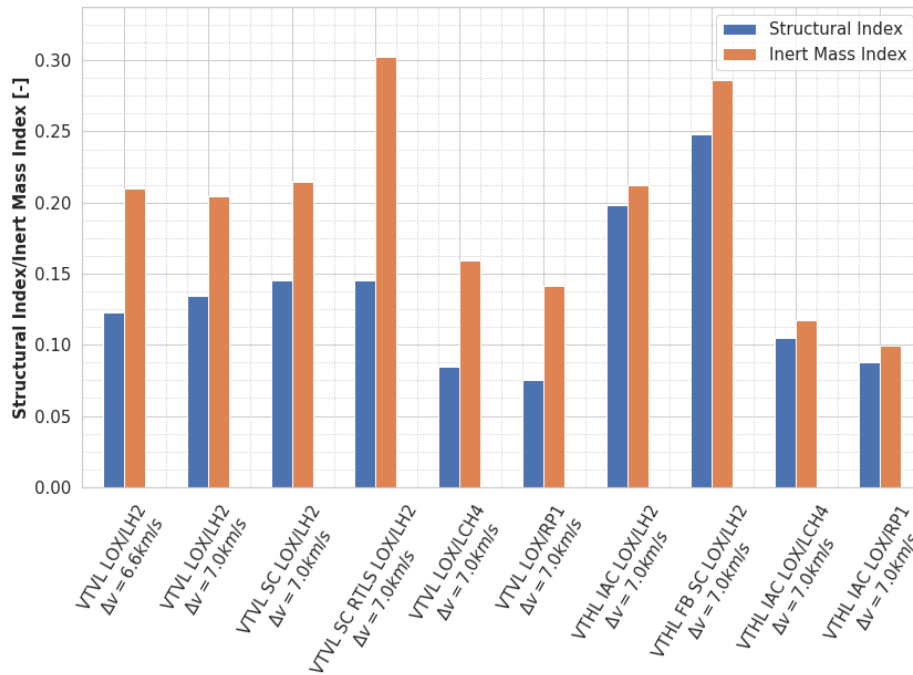


Figure 3.8: Inert Mass and Structural Indices of the conceptual first stages compared [10]

It can be seen how the structural index is higher for hydrogen-based launch vehicles. The difference between these two indices can show which mass contribution is most influential in the design of the RLV: If the inert mass index is much higher than the structural index, the amount of propellant that is required for the controlled descent is more influential on the launcher's performance, meanwhile confrontable values for structural index and inert mass index show that the dry mass is the main driver for the design of the RLV. Usually, a high inert mass index results in a lower performance and a heavier launch vehicle.

Another important aspect to be considered is the estimation of loads, both structural and thermal, impacting the vehicle during the mission.

In Fig. 3.9, the reentry trajectories of the compared launchers, together with the Falcon 9 trajectory (reverse engineered by DLR), are presented. In this graph, the heat flux at stagnation point, calculated with a modified Chapman empirical formula, is reported in the form of isolines as well.

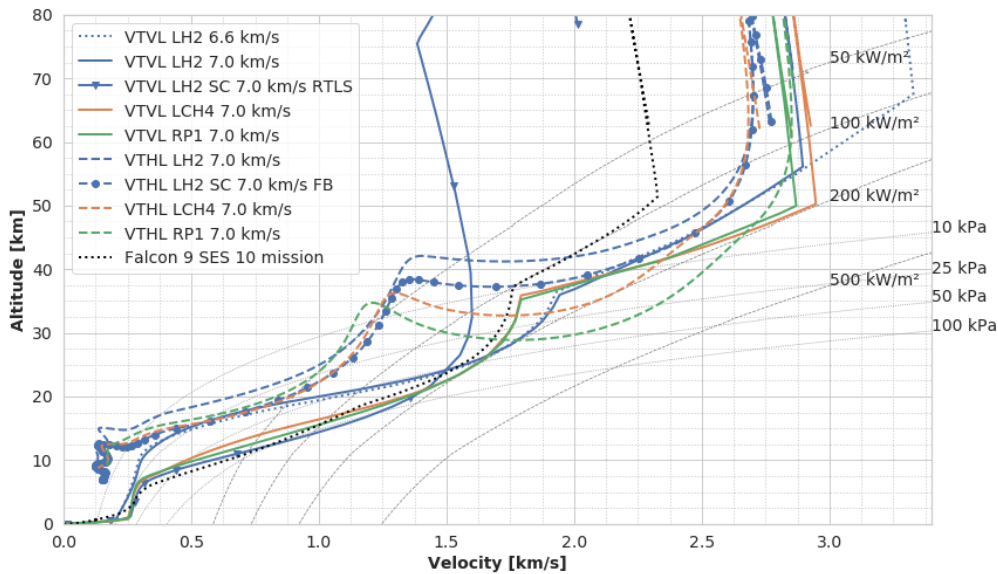


Figure 3.9: Reentry trajectories and heat flux estimation for various reusable solutions, including Falcon 9 [10]

As already mentioned, the reentry burn achieves the required deceleration in the case of VTVL launch vehicles. On the other hand, in case of a return to launch site mission this burn occurs at higher altitudes due to the steeper reentry [10]; a sudden change of the velocity vector occurs. VTHL launch vehicles are characterized by a softer deceleration profile.

In the reentry trajectory profile "it can be clearly seen that the VTVL LVs follow a more or less similar velocity altitude profile due to the fact that a heat flux of 200 kW/m^2 and a maximum dynamic pressure of 200 kPa were set. The former value was based on the SpaceX mission trajectory which experienced a similar maximum heat flux. The VTVL trajectories lie quite close to the 200 kW/m^2 isoline from reentry until around 1.5 km/s . Interestingly, the hydrocarbon LVs experience the first heat flux peak shortly before the begin of the re-entry burn whereas the hydrogen LVs only get close to the 200 kW/m^2 mark during the aerodynamic flight". [10]

3.2 Considerations on Design Parameters

In this section, the most important structural design consideration when designing a reusable launch vehicle will be laid out.

The inert mass fraction highly affects the overall sizing of the reusable rocket, as well as the expendable stages. Structural design has to be efficient from this point of view, but still be robust enough to sustain the applied loads.

In the structural design of a reusable first stage, the following factors are to be considered: [13]

- The adopted construction materials for all parts of the RLV;
- All of the loads that the LV will encounter during its flight, such as engine ignition and cutoff, liftoff loads, maximum aerodynamic pressure, the control manouvers in order to land, retropropulsion loads and general aerodynamic loads;
- All the loads transmitted to the payload during the mission profile, such as acoustic, shock and vibration loads, as well as loads occuring during staging events and payload injection;
- Assembly and manufacturing processes;
- Fast inspections throught nondestructive tests between flight of the reusable launch vehicle;
- Good scheduling of manteinance and repair operations through structural, material fatigue and cycle life controllability;
- Structural mechanisms needed for release of ad-hoc parts for RLVs;
- Management of mass properties on all phases of the mission profile;
- Trasportation loads for refurbishing purposes after flight;
- Loads and stresses caused by the staging event and the landing.

Some of the key aspects in the design of RLVs will be now further detailed, regarding their impact on design and what could be done to solve or alleviate these.

At the moment, metallic materials for the main structures and tanks of reusable launch vehicles are adopted. These materials include good strength to weight ratio alluminums and titanium alloys. The need to increase the propellant mass fraction could arise, and with that composite materials could become an attractive proposition for the main structures of the vehicle and even for the tanks themselves.

When the vehicle encounters aerodynamic loads during its descent, these should not have an inherent risk for the metallic structures that are commonly used in the space transportation sector; the risk could arise if the design of the launcher dictates a choice of new and lighter materials in order to save launch weight. This could have an impact on the overall structural design and the one related to the release mechanisms.

Lighweight composite tanks could bring additional risks to the projects, mainly related to the cryogenic storage of the propellants inside. This is due to the fact that the technology readiness level for cryogenic composite tanks is still low and a lot of research is still to be conducted in order to predict the long-term behaviours of these structures, also due to the inherent reusability of the tanks themselves. Composite tanks arise concern also for the choice of the best bonding and/or fastening techniques to be employed in order to attach them to the main structure of the rocket.

Also to be considered when dealing with reusable launch vehicles that perform return-to-launch-site maneuvers is the additional hardware needed to land the first stage successfully. This hardware includes the aerodynamic surfaces, control surfaces and the landing legs, and this has a negative impacts on the launch mass compared to conventional expendable rockets.

New materials for the design of this additional hardware is needed in order to be competitive in the launch market. In [13] nanomaterial technologies such as large scale nanotube structures are proposed; these kind of structures bring to the table significant gains in material strength-to-weight ratio. Unfortunately, these types of large scale structures are probably far into the future, but in the meantime. new fiber composite materials for the load bearing structures are to be considered as good candidates in terms of material strength to weight ratios.

3.3 Primary Vehicle Structures

When considering the primary structure of a launch vehicle that major factors limit the available dry mass of the LV to about 10/11%, like, for example, the feasible specific impulse (I_{sp}) and economically advantageous gross liftoff weights. A 10% dry-mass fraction equates to a structural mass fraction of about 5%, highlighting the importance of weight control in launch vehicle structural components.

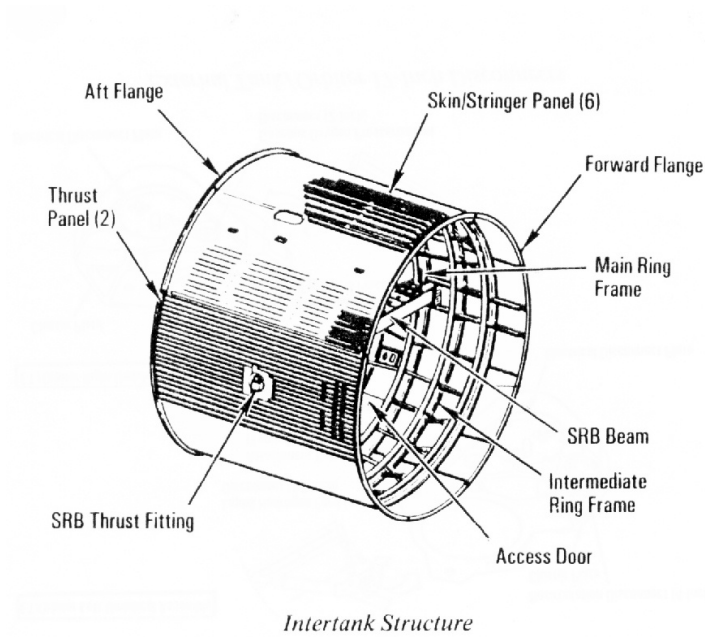


Figure 3.10: Sketch of an intertank structure. *Courtesy of NASA*



Figure 3.11: Falcon 9 thrust structure and engines. *Courtesy of SpaceX*

Among the structural elements that are comprised into the primary structure cryotanks are generally included (a further discussion for these will be reported in the next section), together with possible, depending on the type of RLV considered, aerodynamic surfaces and landing hardware (landing legs, landing gear). The major dry components included in the general design are: [14]

- intertank structures (example reported in Fig. 3.10)
- thrust structures (example reported in Fig. 3.11)
- aerodynamic surfaces (wings, control surfaces, grid fins)

The first structure is called the intertank and is a thin-walled cylindrical section positioned between the LOX and LH₂ tanks inside the LV. Their main function is to carry the launch loads and transfer them to adjacent fuel tanks. Usually the intertank also house various support structures and cutouts for feedthrough holes. The design is comprised of truss structures, skin-string semimonocoque structures and sandwich panels.

As the name suggests, the thrust structure's main function is to transfer and redistribute the engine loads due to thrust throughout the LV. It is subjected to very high loads and needs to operate in a strong vibroacoustic and thermal environment. Some of the configurations could be made up of truss structures, conical shells and reinforced shells. As a thrust structure is made up of different components, those require joining techniques and appropriate manufacturing techniques.

Finally, wings and control surfaces could consist in box beams made up of either from skin stringer panels or honeycomb core panels.

The considered materials of interest for these components are usually graphite-epoxy composite materials or higher temperature graphite-bismaleimides (BMI) composite materials.

Due to the sheer complexity of the behaviour of these materials, especially under critical loadings, both structural and thermal, extensive testing campaigns need to be put in place in order to fully identify mechanical and thermal properties and estimate the possibility of reusability. These tests are useful in order to identify material properties, structural behaviour and general performance. The materials that can

be considered are high strength graphite fibers (e.g. T650 and T1000) together with toughened epoxy (e.g. 8552), cyanate ester and thermoplastic matrices (X3009). The properties need to be identified through testing in both the longitudinal and transverse directions and interlaminar strength. The tests are performed in a wide range of temperatures and moisture levels, together with thermal cycling.

Single laminates also require testing for material characterization, with varying thicknesses and fibers orientations. These tests are performed in order to verify laminate stiffness initial estimations and determine the design strengths of the single sheet of composite material.

Further and more complicated test should be performed, in order to achieve a better understanding of the behaviour of such materials; some of the tests include open hole strength testing, cracking after thermomechanical cycling, liquid oxygen compatibility and through-the-thickness hydrogen permeability.

Another important subject to be considered is joining. One of the biggest criticalities for the primary structures resides in the joints. Therefore, similarly to composite materials, extensive testing campaigns are required, and may include lap shear tests, interlaminar tension tests and pin and bolt tension tests. Lap joints, adhesives, operative temperatures and material configurations (tape or cloth) are extensively tested. The joining components between panels, such as stiffeners and clips are also examined with dedicated tests.

Large scale joint testing is focused on the types of joints used in cryogenic tanks and intertank structures (Y-joints, named after the form they assume in the cross section). Different architectures of Y joints sections, both subscale and full scale should be extensively tested, together with other types of joints as, for example, metal fittings and joints between panels, tank fittings and double lap tank joints.

During a preliminary study of the design of a reusable launch vehicle, a 15% maximum weight margin is considered appropriate, even if the low end of acceptance, because increasing it during the early phases could lead to a first estimation for a larger vehicle. This emphasises the accurate calculation of weight and structural performances during the first phases of a project, together with verification of the producibility of a given structure or component under the predicted weight.

Regarding materials choice, it has been seen that thanks to the large acceptable material configuration availability, a good number of available tradeoffs could be available. However, the best candidates in the use in a reusable launch vehicle appear to be toughened matrix graphite-epoxy for tanks and graphite-bismaleimides for dry structures.

Regarding joints, testing with a damage tolerance design is recommended.

3.4 Reusable Cryogenic Tanks

One of the most important components of the reusable launch vehicle to be developed and integrated is a reusable system of cryogenic tanks. These tanks need to sustain the launch and reentry loads while meeting weight and reusability design requirements.

For expendable stages or vehicles the tanks are simply expelled before entering orbit; in the case of an RLV the tanks are an integral part of the main structure of the craft. These tanks have to store propellant, therefore contribute greatly to the overall mass of the vehicle.

The scope of the adequate technology developments is to design and test different configurations of these components, built using both metallic and composite materials, in order to highlight the merits of such components. In recent years, two main material configurations have been investigated: metallic aluminum-lithium alloys (mainly for liquid oxygen tanks) and composite tanks (mainly for liquid hydrogen tanks). These developments aim at determining if the tanks can be effectively produced and whether technical requirements, such as weight, cost and reusability, can be met.

3.4.1 Aluminum-Lithium Cryogenic Tanks

In [14], the work done by a NASA/Industry cryogenic tank technology program is reported. In this report, the major advantages, disadvantages and design choices for reusable cryogenic tank systems are evaluated.

During the program, aluminum-lithium (Al-Li, example in Fig.3.12) tanks have been built and tested: a 14 feet diameter cryogenic tank was constructed, and included near-net-shape extruded stiffened panels, net-shape spin formed bulkheads and near-net-shape stubs. The chosen material was an Al-Li alloy 2195, with an external cryogenic insulation. The program aimed at developing the technology up to a TRL of 6 (meaning a demonstration/prototype of a system).

Meanwhile, a russian industry partner was developing a similar system using an Al-Li alloy 1460, with some components built with an equivalent of an alloy 2219, for their experimental reusable launch vehicle; the problem with that material was that it was not optimized for its use in a reusable tank.



Figure 3.12: Aluminum-Lithium (Al-Li) cryogenic tank [15]

Another alternative material composition, developed by the US Air Force, is an isotropic aluminum-lithium alloy designated AF(UDRI). It contains more than 2% in weight of lithium, minimum value in order to obtain a 10% of savings in total weight. Its mechanical properties are highly isotropic, comparing it with similar alloys with similar mechanical properties, and this is asset in favour of this material. Furthermore, the fracture toughness is very high in the transverse direction and acceptable in the in-plane direction. Also, compared with a widespread aluminum alloy sych as 7075, fatigue crack growth is significantly better. In Table 3.1, the main mechanical properties of AD(UDRI) are compared with the aforementioned 2195 Al-Li alloy, considering components of comparable geometry. Due to its higher lithium content, alloy AF(UDRI) possesses 3% lower density while having a 6% higher modulus compared to Al2195, making it a great candidate for future use in cryogenic LOX tanks.

	AF(UDRI)	2195
Ultimate strength	548 MPa	552 MPa
Yield Strength	493 MPa	517 MPa
Fracture toughness parameter	44 MPa-m ^{1/2}	37.4 MPa-m ^{1/2}

Table 3.1: Comparison of mechanical properties between AF(UDRI) alloy and Al-Li 2195 alloy [14]

Another criticality in the manufacturing of LOX cryogenic tanks resides in the welding of the selected aluminum-lithium alloy. For example, alloy 2195 can be welded, but second pass welding or weld repair are more difficult to execute. A solution could reside in using an aluminum-silicon alloy filler, that results in better weld repair capabilities. Another method that could be used is friction-stir welding, and it could solve the welding difficulties in aluminum-lithium alloys.

In the end, using Al-Li tanks for LOX cryogenic tanks applications is a robust choice due to the fact that many technological possibilities are available to address the main criticalities of these types of components, both regarding the choice of materials and welding methodologies.

In particular, regarding the choice of material, "alloy 2195 exhibits better cryogenic ductility and significantly greater strength than the conventional alloy for cryogenic tanks, alloy 2219. Alloy 2195 also exhibits a positive fracture toughness ratio when subjected to a range of temperature (from room temperature to cryogenic temperatures), which is an important consideration for cryotanks. Greater strength, coupled with higher modulus and lower density, can lead to significant weight savings. The alloy also has good corrosion resistance, excellent fatigue properties,⁴ can be near-net-shape formed, and, with proper precautions, can be adequately welded." [14]

Regarding the use of the Al-Si alloy filler with welding, caution should be exercised because silicon combines with Al-Li to form AlLiSi phase that absorbs moisture, increasing the risk of stress corrosion crack forming. Stress corrosion tests need to be performed if the need to use this solution arises.

It should also be considered that problems through the thickness properties of constructed thick plates could be present; in that case, the mechanical properties should be identified before use.

Although composite materials are the best solution for the construction of liquid hydrogen tanks, the aforementioned aluminum-lithium tanks could be considered as a backup for this application, together with a titanium honeycomb tank as backup. The problem with Ti structures, particularly the investigated Ti-6Al-4V alloy, is that they are usually susceptible to hydrogen embrittlement; it is therefore necessary to perform an extensive material characterization campaign before this alloy could be used for LH₂ cryogenic tanks.

3.4.2 Composite Cryogenic Tanks

As mentioned before, composite tanks are great candidates for use in liquid hydrogen (LH₂) reusable tanks.

Despite this, several criticalities are present when considering this materials for tanks, such as cycle life, weight and machinability. Studies are underway in order to test subscale composite tanks for material and behaviour characterization, as well as identify different fabrication methodologies for composite cryotanks.

Regarding the fabrication techniques of tanks with composite materials, some of the approaches that could be adopted are:

- simply use carbon fiber cloth layers impregnated with epoxy and formed in the needed shape, having been cured in an autoclave;
- use specific machines in order to apply the graphite/carbon filaments already coated with the epoxy resin and forming it in the desired shape thanks to a mandrel (as seen in Fig. 3.13);
- the fabrication of the tank relies on an honeycomb (or foam) core sandwiched between layers of carbon/graphite epoxy.

Also considering the permeability aspect of LH₂ tanks, extensive testing campaigns resulted in no evidence of relevant cracking or permeability behaviours in LH₂ tanks made by toughened epoxy. Testing consisted in composite tanks being subjected to hundred of cycles at pressure up to ~ 21 bar, with no evidence of leaking.

Of course, the testing campaign is usually performed on subscale cryogenic composite tanks in order to reduce production and testing costs and increase flexibility for considering different material/liner configurations. This in turn creates the problem of scalability, i.e. the uncertainty that a full-scale model of the test tanks will behave similarly and within design constraints.

However, the testing campaign comprises of several thermal and stress cycles for all considered material/construction techniques configurations presented above. By performing approximately 100 cycle tests, the life expectancy of the tank could be verified. The permeability criticality (together with the presence of leaks) is to be monitored during the testing campaign.



Figure 3.13: Example of composite-fibre cryogenic tank from NASA [16]



Figure 3.14: Example of subscale composite-fibre cryogenic tank [17]

In the end, several concerns are present once the use of composite fibre tanks is wanted; among them the cycle life, the producibility and the eventual use of these materials also for the LOX tanks.

As it can be imagined, the cycle life of these components plays a major role, even more than with conventional expendable LVs. Even if preliminary subscale testing campaigns tested for just 5 temperature/pressure cycles, in order to achieve full reusability, for example of 100 temperature/pressure cycles, it can be estimated that the tanks should be tested, verified and certified for at least 200 cycles.

This level of testing is not common, as this level of reusability is not normally needed for expendable components. Another important requirement that composite tanks need to comply with is the ability to withstand possible Micrometeoroids and Orbital Debris (MMOD) impacts due to the large number of flight during their operative life, and also be repairable in some way.

Even though the proposed techniques for fabrication of composite tanks is already commonplace and relatively easy with subscale components, concerns arise once there is the need to consider the full scale tanks required for flight. For instance, autoclaves of appropriate size may not be readily available, therefore the tanks might have to be assembled once some segments have been cured in smaller autoclaves. At this moment, the largest autoclave ever built, by Boeing, has a working diameter of 9.62 meters, while tanks for a reusable launch vehicle might range from approximately 7.62 meters to 12.2 meters. Alternatively, layering the composite by hand might eliminate this problem, but may not be practical for full scale tanks due to their sheer size.

While the primary objective of the design and production of composite tanks is its application to hydrogen tanks, there should be the possibility of using the same materials also for the liquid oxygen tanks. It is usually considered not the best approach due to the inherent risk of using composites with oxygen, but, even with aluminum or stainless steel materials which are widely used in LOX tanks, these materials are prone to burn once ignited. Furthermore, using composites instead of metallic materials does not bring a lot more risks, as the interaction behaviour is similar.

3.5 Thermal Protection and Insulation Systems

When considering reusable launch vehicles, and subsequently their primary structure and cryogenic tanks, the need for protection for thermal loads arises. Therefore Thermal Protection Systems (TPS) for reusable launch vehicles are needed in these vehicles. The TPS must be constructable, lightweight, cost effective and be certified for at least 100 cycles (to comply with imposed reusability requirements). When talking about cost effectiveness in an RLV program, the first thing that comes to mind are maintenance and inspection costs; as previously mentioned, when compared with the not so cost effective Space Shuttle program, improvements are needed to be competitive in today's space transportation market in terms of launch costs.

Continuing to consider the Space Shuttle program, in which a fully reusable TPS was showcased during its lifespan, the main metallic structure did not exceed temperature limits and heat leaks into the tanks did not occur thanks to the TPS. However, there have been situations in which various parts of the TPS protecting the vehicle had been exposed to exceeding temperature limits, and this caused some parts to exhibit embrittlement, cracking and flaking of the coating. In addition to this, damage caused during landing or orbital debris occurred, highlighting the lack of thermal protection system robustness, causing the need of extremely high manhours and resources in order to repair the TPS itself.

In the Space Shuttle, another problem arose after every mission: re-waterproofing. Waterproofing of the TPS was necessary in order to prevent moisture absorption within the TPS, which would increase overall weight therefore reducing payload weight. After every mission, as the vehicle reached temperatures that degrade the waterproofing agent, every part of the TPS needed to be rewaterproofed. This increased the turnaround time significantly and consumed resources.

Both of these problems must be addressed and resolved in the design of a future reusable launch vehicle.

Together with external thermal protection systems, cryogenic insulation is needed for the liquid oxygen and liquid hydrogen reusable tanks. In fact, insulation of fuel tanks is needed, either internally or externally of the tanks, in order to prevent moisture buildups in the air forming ice on the cryotanks (in the early stages of the

mission). Ice buildups could increase the weight of the vehicle at launch and also, if large chunks of ice detach from the tanks, create some serious damage to other parts of the vehicle. On the other hand, insulation also combats the heat from the atmosphere in reaching the liquid propellant in the tanks, vaporizing it before takeoff.

In Fig. 3.15, two possible layered configurations are reported, one with the insulation inside of the tank and one positioned on the outside. One of the main concerns for research is finding a way of easily and rapidly removing the TPS when necessary; as of today it can be easily bonded to the tanks, but a better methodology for increased maintainability should be developed to further reduce turnaround times and costs.

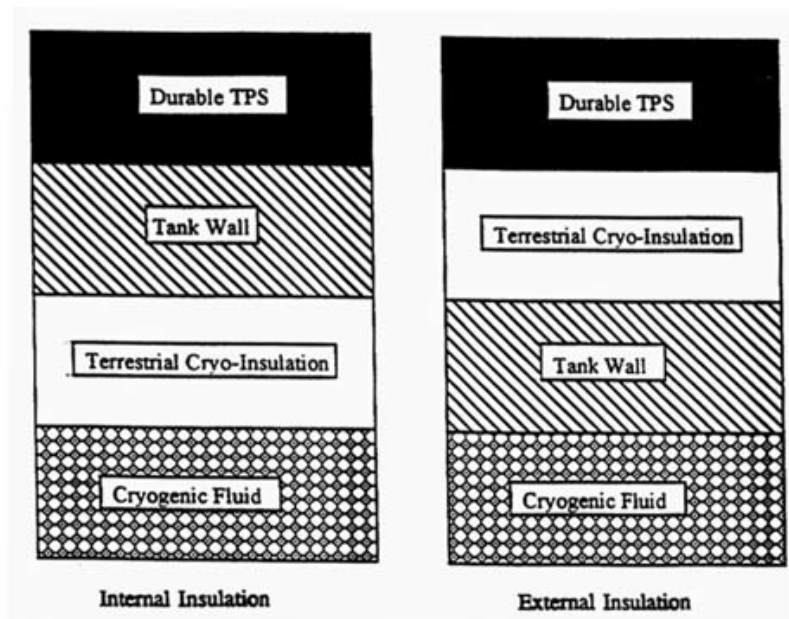


Figure 3.15: Examples of thermal protection system configurations for cryogenic tanks [14]

3.5.1 TPS Materials Research Programs

Among NASA and space industry research program, some solutions that will improve the performance of thermal protection systems in future RLVs have been identified.

One of them focused on composite refractory TPSs (carbon/silicon carbide). These materials have a good resistance to atmospheric conditions, such as rain or erosion by particle impact, moisture and frost. These materials could bring a 15 to 25% reduction in weight with respect to the Space Shuttle ceramic tiles using lighter weight insulation. Large size testing can be performed with realistic structural, thermal, vibrational and oxidation conditions, as well as testing extreme environmental conditions like low/high speed particle impacts and general weather exposure.

Another program focused on an innovative insulation blanket that could be used for the upper part of the vehicle (in reduced thermal stress areas); examples include the AFRSI (Advanced Fibrous Refractory Surface Insulation, made of Nexted 440 fabric and alumina capable of withstanding $\sim 1100^{\circ}\text{C}$) and CFBI (Composite Flexible Blanket Insulation, made of AFRSI with an added multi layer insulation for additional insulation capabilities).

Regarding joining/bonding techniques for these materials, adhesive bonding with a silicon adhesive can be considered. This type of joining has the advantages of being reliable, having a good water resistance, having no risk of thermal short and relatively high bond line strength. On the contrary, they are complex to install and/or remove and difficulty of inspection.

Mechanical fastening techniques can be also considered, like for example floating nut plates and capstans. These bring ease of inspection and installation, good resistance to waterproofing agents and high temperature tolerance, but also increased risk of thermal shorts and increased weight and water intrusion.

Further types of material configuration for TPS can be adopted for the most stressed part of the vehicle, the underside. Among them the AETB (Alumina Enhanced Thermal Barrier, tiles with the inclusion of alumina fibers able to support $\sim 1450^{\circ}\text{C}$) and SIRCA (Silicon Impregnated Reusable Ceramic Ablator, a silica tile impregnated with an ablative silicone with good reusability potentialities for the vehicle leading edge and nosecone). New generation coated ceramic tiles have better

impact and damage resistance capabilities, especially the TUF_I coating (Toughened Uni-piece Fibrous Insulation, a toughened tile coating).

Yet another type of materials are ceramic matrix composites, such as C/SiC (carbon fiber reinforced silicon carbide matrix composites), SiC/SiC (silicon carbide/silicon carbide composites) and ACC (advanced carbon/carbon composites). These ceramic matrix composites are able to protect the leading edges of the vehicle during the re-entry phase and are able to withstand up to 1650°C, also weighting less than the respective counterparts used in the Space Shuttle program.

In the following tables the main design concepts of thermal protection systems for different parts of the vehicle, together with the concerns for each one, are reported.

Concept	Attributes	Concerns/More Data Required
<i>Nose Cone and Leading Edges</i>		
Advanced Carbon/Carbon	Higher strength than reinforced carbon-carbon; used on orbiter.	Oxidation-effects data required. High thermal conductivity may require complex, heavy attachment mechanism. Rain-erosion resistance data required.
Carbon/SiC or SiC/SiC	Good potential. No coatings required (oxidation resistant).	High thermal conductivity. Rain-erosion resistance data required. Development tests required.
SIRCA	Easy to produce in appropriate size. Low thermal conductivity. Allows backface attachment.	Reusability and rain-erosion resistance data required.
AETB tiles with TUF _I coating	Easy to produce in appropriate size. Low thermal conductivity. Allows backface attachment. Low fabrication cost.	Data required on temperature resistance. Requires waterproofing. Lack of appropriate thermal cycling data. Data required on rain-erosion resistance of coating.
AETB/TUF _I	Best reusable surface insulation tile material/coating system. Attachment by bonding. Fabrication analogous to shuttle tile.	Requires waterproofing. Requires gap fillers.
C/SiC or SiC/SiC standoff panels	Potential low weight. Thermally stable.	High cost. Standoff design for thermal expansion. Development tests required.
Metallic (superalloy)	Robust and damage tolerant. Protected insulation. Panel-to-panel overlap minimizes gap seal problems. Design refined over many years.	Attachment must allow for thermal expansion. Heat transfer through attachment.
TABI	Best blanket insulation. Attachment by bonding, no heat shorts. Potential 2,000°F reuse. Larger size than tile insulation.	Requires waterproofing. Protective coating performance data required.

Figure 3.16: TPS concepts for nosecone and leading edges [14]

Concept	Attributes	Concerns/More Data Required
<i>Upper (Leeward) Surfaces</i>		
NEXTEL/AFRSI	Lower cost than TABI. Better insulator than TABI. Flight experience on orbiter.	Requires waterproofing. Coating performance data required. Stitching needs more development.
Titanium Honeycomb	Robust and damage tolerant. Lightweight. Large panel sizes. Panel-to-panel overlap minimizes gap seal problems.	1,000°F limit.
Polybenzimidazole (polymer) Felt	High temperature polymer (800°F). Low density. Low thermal conductivity. Attached by bonding.	Higher cost than Nomex. Lack of test data. No data on waterproofing.
<i>Thermal Insulation</i>		
Internal Multiscreen Insulation	Good potential.	High cost. Unproven concept. Development testing required.
Ceramic Fiber Bat	Low cost, commercial item. Can be encapsulated to protect from elements. Material change with reduced temperature for maximum efficiency.	Settling under vibratory loading and thermal cycling.
Reflective-coated Fiber Bat	Good potential.	Higher cost than fiber bat. Test data required.
Multilayer Insulation	Mature concept.	Most efficient in vacuum; less efficient in air.
<i>Cryogenic Insulation</i>		
External Foam-Filled Honeycomb	Failsafe design for foam. TPS attachment by bonding to honeycomb. Minimizes foam cracking.	High TPS to cryogenic insulation interface temperature due to lack of heat sink.
<i>Note: Standoff panels could be attached directly to the tank walls through holes in the cryogenic insulation. Subsequently, holes could be closed out with pour foam.</i>		
Internal Fiber-Reinforced Foam Panels with Fiberglass Liner	Provides heat sink capability of tank wall for entry heating. Uses water (CO ₂)-blown foam which causes no stratospheric ozone depletion.	Ice formation on exterior of LH ₂ tank wall because of hydrogen permeability. Inspection/repair requires access to tank interior, which can be source of contamination. Not suitable for LOX tank because not LOX compatible.

Figure 3.17: TPS concepts for upper edges, thermal insulation and cryogenic insulation [14]

Another additional type of thermal protection system fore RLVs is the Metallic Thermal Protection System (MTPS). These have been developed since 1977, and offer several advantages compared to classic ceramic tiles, among them: [18]

- lower weight but higher reliability
- better durability and shock resistance

- lower total periodic costs
- same thermal expansion coefficient as the primary structure

As already mentioned, both during ascent and reentry, the reusable launch vehicle is subjected to severe thermal radiation and there is the possibility of high speed MMOD impact. With that said, some of the requirements for the MTPS should be:

- good resistance to high temperatures and oxidation
- good environment resistance
- lightweight but with good mechanical strength
- low cost and good repairability
- ability of ease of fabrication techniques and manufacturing of materials
- availability of effective joining techniques

As seen above, when considering metallic materials, the RLV can be broken down in three different areas of interest for TPSs. MTPS are usually adopted for low/intermediate temperature regions (588-1473 K).

The materials that could be considered are titanium based alloys for the low temperature regions, nickel based alloys for the intermediate temperature regions and intermetallics, like titanium-aluminum based alloys, in the 1000 K temperature regions.

Nickel based superalloys possess the best properties and highest density, while titanium based boast low density values while having the lowest resistance to high temperatures among these materials. Multilayer composites can be introduced into these materials in order to improve high temperature properties and improve practicality, and using intermetallics as a toughener to maintain high temperature strength and creep resistance.

In recent years, thanks to efficiency advancements of computers, computational based calculations using, for example, finite element solvers have allowed for a better understanding of material and structural behaviours.

These capabilities resulted in reduced costs for the design of structures and material characterizations, as less testing is needed in order to validate a certain designed structure. As a result, engineering practices have changed: one of the first phases of any project that requires a new structural design has become an iterative process, thanks to finite element analysis, in which different configurations can be virtually tested, resulting in savings in both project overall cost and time needed to design, assemble and use a structure.

That being said, the computational models and solvers need to accurately predict the real life behaviour of a structure in order to be useful in the design process. Solutions given by analyses performed on structures of which analytical solutions are already available in the literature could be one way of validating the accuracy of a solver.

Today's and future interests and research rely on the accurate prediction of the behaviour of structures of which analytical solutions are not available, mainly due to the difficulty of the problem. One example is the nonlinear behaviour of structures subjected to large deflections or with geometrical imperfections. Examples of these structures could be found in the ones mentioned in the previous chapters. In fact, accurate prediction of the whole range of behaviours of thin walled shells are strictly linked with their nonlinear behaviour, as buckling phenomena can easily occur in badly-designed structures. These include the cryogenic tanks and the primary structures currently employed in launch vehicles.

It needs to be reported that these kinds of analyses require extreme computational capabilities, costing the designer both money and time. An easy and cost effective way of producing relevant results is by using a commercial FEM software, like ABAQUS for example. These software yield useful results in the first parts of a project, as they give a rough idea of which configurations could be most suitable for a given project. The main drawback, in fact, is the cost/accuracy ratio: in order to obtain highly accurate results, an excessive computational cost is required.

The main solution that is proposed in this work, which will be explained more in detail in Chapter 4, is the Carrera Unified Formulation (CUF), a mathematical unified formulation that allows for reduced computational cost of difficult-to-solve structural models without sacrificing accuracy. Some examples of the capabilities of this formulation, together with analyses of thin-walled shells, similar to the ones that have been discussed before in this chapter, will be reported in Chapter 5.

Chapter 4

The Carrera Unified Formulation for Nonlinear Problems

In the following chapter, the Unified Formulation that will be employed in the present work for the subsequent analyses of thin-walled structures will be presented. More precisely, the Carrera Unified Formulation (CUF) provides 1D and 2D theories that expand on the classical structural theories (for example those of Euler, Mindlin, Kirchhoff, etc.), mainly by expressing the displacement field over the cross-sections of beams and along the plate (or shell) thickness in terms of base functions whose forms and orders are arbitrary; the CUF also exploits a condensed notation. This condensed notation allows the expression of *fundamental nuclei* (FNs) of all the Finite Element Method (FEM) matrices and vectors involved.

The FNs are comprised of essentially a few mathematical statements, and their forms are independent of the theory of structures that is employed. The FNs are derived from the 3D elasticity equations via the principle of virtual displacements (PVD). Fig. 4.2 shows the essential features of the CUF. The strong form of the equilibrium equations allows one to derive a compact formulation for the fundamental nucleus. The nine elements of the FN can be written using only 2 terms.

In this figure, k_{xx} and k_{xy} are reported. All the remaining terms can be derived by

a permutation of the indexes. This compact formulation is used to derive the 3D, 2D and 1D models in weak form. [19]

This formulation was first introduced in a 1995 paper [20] and its use-cases have grown and evolved ever since. In fact, some of the applications of the formulation include, but are not limited to: Equivalent Single Layer (ESL), Layer-Wise (LW) and Zig-Zag (ZZ) models, shell FE models, performing static and dynamic analyses of structures (thermal loads could be included in the formulation), thin-walled structures with the reinforcements (of interest for the present work), buckling phenomena, multifield applications, aeroelasticity problems (even in the supersonic range), flutter analysis, rotor dynamics, electro mechanical analysis, biomechanical applications, stability of structures, failure analysis and, of great relevance for the present thesis, geometrically nonlinear analysis.

Interested readers are referred to [19] for a complete overview of the CUF and its many applications. In the following chapters the focus will shift only on a small fraction of applications, mainly, buckling, geometrically nonlinear problems and stability of 2D shell structures (with structural reinforcements), which could accurately represent, in a preliminary analysis environment such as the one considered here, the cylindrical structures used in launch vehicles (LVs).

The steps that are to be performed in a nonlinear analysis using the CUF will now be presented. More specifically: the fundamental relations, the PVD written in terms of FNs, nonlinear displacement-strain relations, the Green-Lagrange strain tensor, the CUF coupling with the FEM, the secant and tangent stiffness matrices, nonlinear equilibrium states and the Newton-Raphson linearization using the arc-length method.

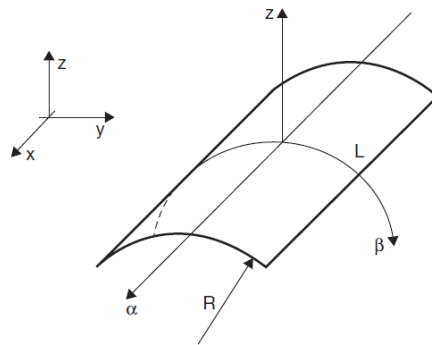


Figure 4.1: Generic cylindrical shell structure and its reference system (α, β, z) , akin to those that will be used in the analyses [19]

Equilibrium equations in Strong Form $\rightarrow \delta L_i = \int_V \delta u k u dV + \int_S \dots dS$

$$\underbrace{\begin{bmatrix} k_{xx} & k_{xy} & k_{xz} \\ k_{yx} & k_{yy} & k_{yz} \\ k_{zx} & k_{zy} & k_{zz} \end{bmatrix}}_k \underbrace{\begin{Bmatrix} u_x \\ u_y \\ u_z \end{Bmatrix}}_u = \underbrace{\begin{Bmatrix} p_x \\ p_y \\ p_z \end{Bmatrix}}_p$$

$$k_{xx} = -(\lambda + 2G) \partial_{xx} - G \partial_{zz} - G \partial_{yy};$$

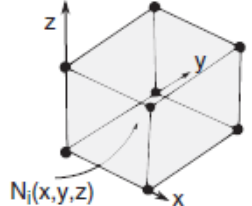
$$k_{xy} = -\lambda \partial_{xy} - G \partial_{yx};$$

$$k_{xz} = \dots$$

$$\lambda = (E\nu)/[(1+\nu)(1-2\nu)]; \quad G = E/[2(1+\nu)]$$

$u = u(x, y, z)$
 $\delta u = \delta u(x, y, z)$

The diagonal (e.g. k_{xx}) and the non-diagonal (e.g. k_{xy}) terms can be obtained through proper index permutations.

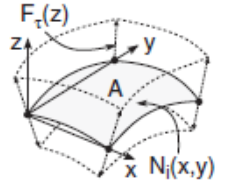


3D FEM Formulation $\rightarrow \delta L_i = \delta u_j k^{ij} u_i$

$$k_{xx}^{ij} = (\lambda + 2G) \int_V N_{j,x} N_{i,x} dV + G \int_V N_{j,z} N_{i,z} dV + G \int_V N_{j,y} N_{i,y} dV;$$

$$k_{xy}^{ij} = \lambda \int_V N_{j,y} N_{i,x} dV + G \int_V N_{j,x} N_{i,y} dV$$

$u = N_i(x, y, z) u_i$
 $\delta u = N_j(x, y, z) \delta u_j$



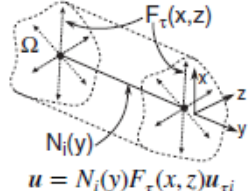
2D FEM Formulation $\rightarrow \delta L_i = \delta u_{sj} k^{rsij} u_{ri}$

$$k_{xx}^{rsij} = (\lambda + 2G) \int_{\Omega} N_{i,x} N_{j,x} d\Omega \int_h F_{\tau} F_s dz$$

$$+ G \int_{\Omega} N_i N_j d\Omega \int_h F_{\tau,z} F_{s,z} dz + G \int_V N_{i,y} N_{j,y} d\Omega \int_h F_{\tau} F_s dz;$$

$$k_{xy}^{rsij} = \lambda \int_{\Omega} N_{i,y} N_{j,y} d\Omega \int_h F_{\tau} F_s dz + G \int_{\Omega} N_{i,x} N_{j,y} d\Omega \int_h F_{\tau} F_s dz$$

$u = N_i(x, y) F_{\tau}(z) u_{\tau i}$
 $\delta u = N_j(x, y) F_s(z) \delta u_{sj}$



1D FEM Formulation $\rightarrow \delta L_i = \delta u_{sj} k^{rsij} u_{ri}$

$$k_{xx}^{rsij} = (\lambda + 2G) \int_l N_i N_j dy \int_A F_{\tau,x} F_{s,x} dA$$

$$+ G \int_l N_i N_j dy \int_A F_{\tau,z} F_{s,z} dA + G \int_l N_{i,y} N_{j,y} dy \int_A F_{\tau} F_s dA;$$

$$k_{xy}^{rsij} = \lambda \int_l N_{i,y} N_{j,y} dy \int_A F_{\tau} F_{s,x} dA + G \int_l N_i N_{j,y} dy \int_A F_{\tau,x} F_s dA$$

$u = N_i(y) F_{\tau}(x, z) u_{\tau i}$
 $\delta u = N_j(y) F_s(x, z) \delta u_{sj}$

- CUF leads to the automatic implementation of any theory of structures through 4 loops (i.e. 4 indexes):
- τ and s deal with the functions that approximate the displacement field and its virtual variation along the plate/shell thickness ($F_{\tau}(z), F_s(z)$) or over the beam cross-section ($F_{\tau}(x, z), F_s(x, z)$);
 - i and j deal with the shape functions of the FE model, (3D: $N_i(x, y, z), N_j(x, y, z)$; 2D: $N_i(x, y), N_j(x, y)$; 1D: $N_i(y), N_j(y)$).

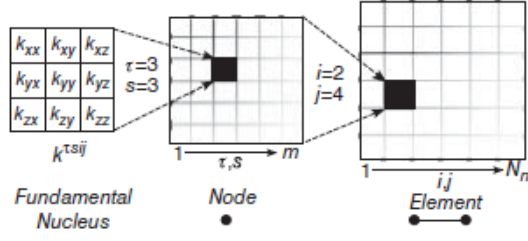


Figure 4.2: A schematic description of the CUF and the related fundamental nucleus of the stiffness matrix for 3D, 2D and 1D models [19]

4.1 Fundamental Relations

In this section, the fundamental equations for continuous and deformable bodies are reported. These equations are given for the linear case.

At a generic point Q of a volume V , the nine stress components must fulfill the following differential equilibrium conditions:

$$\begin{aligned}\frac{\partial\sigma_{xx}}{\partial x} + \frac{\partial\tau_{xy}}{\partial y} + \frac{\partial\tau_{zx}}{\partial z} &= g_x \\ \frac{\partial\tau_{xy}}{\partial x} + \frac{\partial\sigma_{yy}}{\partial y} + \frac{\partial\tau_{zy}}{\partial z} &= g_y \\ \frac{\partial\tau_{xz}}{\partial x} + \frac{\partial\tau_{yz}}{\partial y} + \frac{\partial\sigma_{zz}}{\partial z} &= g_z\end{aligned}\tag{4.1}$$

where g_x , g_y and g_z represent the inertial forces. Equilibrium conditions that are related to rotations along the body axes lead to the Cauchy theorem:

$$\sigma_{xz} = \sigma_{zx} \quad \sigma_{yz} = \sigma_{zy} \quad \sigma_{xy} = \sigma_{yx}\tag{4.2}$$

This equilibrium equations can be rearranged and written in vectorial form, as such:

$$\boldsymbol{\sigma} = \mathbf{b}g\tag{4.3}$$

where \mathbf{b} is the linear differential operator of the strain-displacements relations:

$$\boldsymbol{\sigma} = \begin{bmatrix} \partial/\partial x & 0 & 0 \\ 0 & \partial/\partial y & 0 \\ 0 & 0 & \partial/\partial z \\ \partial/\partial z & 0 & \partial/\partial x \\ 0 & \partial/\partial z & \partial/\partial y \\ \partial/\partial y & \partial/\partial x & 0 \end{bmatrix}\tag{4.4}$$

In the simple case of linear problems (when, after performing the analysis, the undeformed and deformed configurations do not differ greatly) the strain components, e.g.

$\varepsilon_{xx}, \varepsilon_{yy}, \varepsilon_{zz}, \gamma_{xy}, \gamma_{zx}$ and γ_{zy} are associated to the displacement components u_x, u_y and u_z through the linear differential operator \mathbf{b} ; as such the compact formulation of the strains in vectorial form becomes

$$\boldsymbol{\varepsilon} = \mathbf{b}\mathbf{u} \quad (4.5)$$

4.1.1 Hooke's Law

Hooke's Law determines the physical relation between stress and strain components through stiffness coefficients, as

$$\boldsymbol{\sigma} = \mathbf{C}\boldsymbol{\varepsilon} \quad (4.6)$$

For *isotropic materials*, the stiffness coefficients are

$$\mathbf{C} = \begin{bmatrix} C_{11} & C_{12} & C_{12} & 0 & 0 & 0 \\ C_{21} & C_{11} & C_{12} & 0 & 0 & 0 \\ C_{21} & C_{21} & C_{11} & 0 & 0 & 0 \\ 0 & 0 & 0 & C_{44} & 0 & 0 \\ 0 & 0 & 0 & 0 & C_{44} & 0 \\ 0 & 0 & 0 & 0 & 0 & C_{44} \end{bmatrix} \quad (4.7)$$

where $C_{11} = 2G + \lambda$, $C_{12} = C_{21} = \lambda$ and $C_{44} = G$. The coefficients in these relations are

$$G = \frac{E}{2(1 - \nu)} \quad \lambda = \frac{\nu E}{(1 + \nu)(1 - 2\nu)} \quad (4.8)$$

In the case of *orthotropic materials*, such as carbon fibre composites, the stiffness coefficients depend on the directional mechanical properties of the material (e.g. the Poisson's ratios and Shear moduli). The matrix formulation is

$$\mathbf{C} = \begin{bmatrix} C_{11} & C_{12} & C_{13} & 0 & 0 & 0 \\ C_{21} & C_{22} & C_{23} & 0 & 0 & 0 \\ C_{31} & C_{32} & C_{33} & 0 & 0 & 0 \\ 0 & 0 & 0 & C_{44} & 0 & 0 \\ 0 & 0 & 0 & 0 & C_{55} & 0 \\ 0 & 0 & 0 & 0 & 0 & C_{66} \end{bmatrix} \quad (4.9)$$

Expanding the passages above to the nonlinear case, as far as the geometrical relations are considered, the Green-Lagrange nonlinear strain components are used. Therefore, the displacement-strain relations are expressed as

$$\boldsymbol{\varepsilon} = \boldsymbol{\varepsilon}_l + \boldsymbol{\varepsilon}_{nl} = (\mathbf{b}_l + \mathbf{b}_{nl}) \mathbf{u} \quad (4.10)$$

where \mathbf{b}_l is the aforementioned \mathbf{b} linear differential operator and \mathbf{b}_{nl} is the nonlinear differential operator, which is here reported for completeness:

$$\mathbf{b}_{nl} = \begin{bmatrix} \frac{1}{2} (\partial_x)^2 & \frac{1}{2} (\partial_x)^2 & \frac{1}{2} (\partial_x)^2 \\ \frac{1}{2} (\partial_y)^2 & \frac{1}{2} (\partial_y)^2 & \frac{1}{2} (\partial_y)^2 \\ \frac{1}{2} (\partial_z)^2 & \frac{1}{2} (\partial_z)^2 & \frac{1}{2} (\partial_z)^2 \\ \partial_x \partial_z & \partial_x \partial_z & \partial_x \partial_z \\ \partial_y \partial_z & \partial_y \partial_z & \partial_y \partial_z \\ \partial_x \partial_y & \partial_x \partial_y & \partial_x \partial_y \end{bmatrix} \quad (4.11)$$

where $\partial_x = \frac{\partial(\cdot)}{\partial x}$, $\partial_y = \frac{\partial(\cdot)}{\partial y}$ and $\partial_z = \frac{\partial(\cdot)}{\partial z}$ for compactness.

Regarding the development of geometrically nonlinear theories, such as finite, moderate and small rotations and the von Kàrmàn approximations [21], these have been employed extensively in commercial finite element codes. Despite this, it should be noted that those approximations of geometrically nonlinear relations

can lead to different application ranges with certain limiting conditions. As an example, the von Kàrmàn type theory assumes that only those nonlinear terms related to the in-plane partial derivatives of the transverse displacement are reserved in the strain-displacement relation, which could provide acceptable predictions for thin plates or shells with only moderate rotations. However, the accuracy of von Kàrmàn approximations could be not ensured for thick structures with large rotations, especially in the case of shear loadings [22]. Thus, some investigations contain all nonlinear terms of the Green-Lagrange strain tensor in the framework of the higher-order and refined models to conduct the full geometrically nonlinear analysis. [23]–[25]

4.2 Finite Element Approximation

After defining the fundamental relations needed in the formulation, it will now be shown how the finite element formulation is implemented in the CUF. There will be reported both the 1D and the 2D model formulation.

For a 1D model, the tridimensional displacement field $\mathbf{u}(x, y, z)$ within the CUF framework can be seen as an expansion of the primary unknowns, i.e.

$$\mathbf{u}(x, y, z) = F_s(x, y)\mathbf{u}_s(y) \quad \text{with } s = 1, 2, \dots, M \quad (4.12)$$

where F_s are the generalized functions on the cross-section, u_s is a vector of generalized displacements along the beam axis, M is the order of the expansion in the thickness direction and s is the assumed index of the summation.

Of course, the choice of the F_s functions is key in determining the class of the 1D CUF model that is required. For example, in [26], a nine-point Lagrange polynomials (L9) was used to approximate the cross sectional displacement field. The field given by one single approximation is composed of the three components u_x , u_y and u_z ; for example, u_x is

$$u_x = F_1U_{x_1} + F_2u_{x_2} + F_3u_{x_3} + F_4u_{x_4} + F_5u_{x_5} + \dots + F_9u_{x_9} \quad (4.13)$$

where u_{x_1}, \dots, u_{x_9} are the displacement variables of the problem itself; the same structure can be applied to write out the u_y and u_z components. These describe the traslational components of each of the 9 points of the L9 element. This is of course an approximation, but it has been proven to be a good candidate for studying a wide range of classes of structures. [27]

The Finite Element Method, or FEM, is used in order to perform a discretization of a structure along its y -axis, when considering a 1D model. In fact, the generalized displacement vector can be written as

$$\mathbf{u}_s = N_j(y)\mathbf{q}_{sj} \quad \text{with } j = 1, 2, \dots, p + 1 \quad (4.14)$$

with $N_j(y)$ being the j -th 1D shape function, p being the order of these shape functions and j as the index of summation. The vector of the finite element nodal parameters \mathbf{q}_{sj} is defined as

$$\mathbf{q}_{sj} = \begin{bmatrix} q_{x_{sj}} & q_{y_{sj}} & q_{z_{sj}} \end{bmatrix}^T \quad (4.15)$$

It's interesting to note how the choice of the cross-section polynomial sets for the Lagrangian Expansion kinematics is independent of the choice of the beam finite elements used in the beam axis.

For what concerns the 2D models, the 3D displacement field $\mathbf{u}(\alpha, \beta, z)$ within the CUF framework can be expanded as a set of thickness functions which depend only on the thickness coordinate z . The corresponding variables depend only on the in plane coordinates α and β . In fact, the displacement field can be seen as

$$\mathbf{u}(\alpha, \beta, z) = F_s(z)\mathbf{u}_s(\alpha, \beta) \quad \text{with } j = 0, 1, \dots, N \quad (4.16)$$

similarly to the 1D beam case. N represents the order of expansion in the thickness direction. Continuing to relate to the work proposed in [26], the chosen Lagrange expansion function is the three-node quadratic (LD2).

In this case, the 2D shell structure can be discretized using the FEM in the $\alpha - \beta$ plane. Moreover, the generalized displacement vector $\mathbf{u}_s(\alpha, \beta)$ is approximated as

$$\mathbf{u}_s(\alpha, \beta) = N_j(\alpha, \beta)\mathbf{q}_{sj} \quad \text{with } j = 0, 1, \dots, p + 1 \quad (4.17)$$

where, similarly to the 1D case, N_j indicated the j -th shape function, p the order of said functions and j is the repeated index of the summation. In this case, the FE modal parameters vector is defined as

$$\mathbf{q}_{sj} = \begin{bmatrix} q_{\alpha_{sj}} & q_{\beta_{sj}} & q_{z_{sj}} \end{bmatrix}^T \quad (4.18)$$

In [26] and also in this work, the classical 2D nine node quadratic finite elements (Q9) shape function will be used. A better visual understanding of the models that will be used to study the shell structures throughout with thesis work is reported in Figure 4.3: here the F_s expansion functions can be seen highlighted in red (used both for the approximation of the cross section of the 1D model and the thickness of the 2D shell model) while the N_j shape functions (for the beam axis and the 2D midsurface) are highlighted in blue.

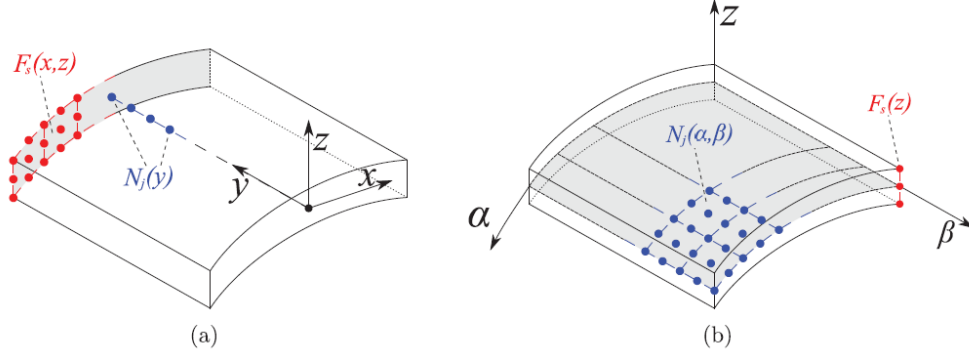


Figure 4.3: Employed approximations of the 1D (a) and 2D (b) models of a reference shell structure [26]

Finally, after defining the CUF relations (Eq. 4.12 and Eq. 4.16) and the FEM relations (Eq. 4.14 and Eq. 4.17) and introducing them into Eq. 4.10, the strain vector can be rewritten as

$$\boldsymbol{\varepsilon} = \left(\mathbf{B}_l^{sj} + \mathbf{B}_{nl}^{sj} \right) \mathbf{q}_{sj} \quad (4.19)$$

where \mathbf{B}_l^{sj} and \mathbf{B}_{nl}^{sj} are, respectively, the linear and nonlinear algebraic matrices with CUF and FEM formulations. The explicit form of these matrices can be found in [23] concerning 2D models, and are not reported here for the sake of conciseness.

4.3 Nonlinear Equilibrium Equations

To easily derive the nonlinear static equilibrium equations, the principle of virtual work (PVW) can be employed. The principle states that, for an infinitesimal virtual displacement that satisfies the given geometrical constraints, the virtual variation of internal work (∂L_{int}) must be equal to the virtual variation of the external work given by the loads (∂L_{ext}), meaning

$$\partial L_{int} = \partial L_{ext} \quad (4.20)$$

where ∂ represents the virtual variation operator.

Nonlinear differential problems emerge once large deflection of elastic systems analysis are considered. The equilibrium conditions can be written as a system of nonlinear algebraic equations; so, using both the CUF and FEM relations previously reported (for the 2D shell case Eq. 4.16 and Eq. 4.17) together with Eq. 4.20, the finite element approximation can be rewritten with a unified expression, as

$$\mathbf{K}_s^{ij\tau s} \mathbf{q}_{sj} - \mathbf{p}_{sj} = \mathbf{0} \quad (4.21)$$

where \mathbf{p}_{sj} are the Fundamental Nuclei of the vector of the nodal loads and $\mathbf{K}_s^{ij\tau s}$ is the secant stiffness matrix. The above equation represents a set of three algebraic equations.

Once the approximation order has been chosen and the element secant stiffness matrix has been obtained, it can be assembled in the classical way of FEM. [19] By assembling the finite elements in the CUF framework, the nonlinear algebraic governing equations can be expressed as

$$\mathbf{K}_s \mathbf{q} - \mathbf{p} = \mathbf{0} \quad (4.22)$$

with \mathbf{K}_s , \mathbf{q} and \mathbf{p} being the global assembled finite element arrays of the whole structure (in this case, the 2D shell structure). For the explicit expressions of these arrays, the reader is referred once again to [19].

4.3.1 Newton-Raphson linearization with path-following constraint

The starting point for any FE analysis of geometrically nonlinear problems is Eq. 4.22. From this point, the equations are usually solved using an incremental linearized scheme, typically the Newton-Raphson method (tangent method). Using this method, Eq. 4.22 can be rewritten as

$$\boldsymbol{\varphi}_{res} \equiv \mathbf{K}_s \mathbf{q} - \mathbf{p} = 0 \quad (4.23)$$

where $\boldsymbol{\varphi}_{res}$ is a vector of the residual nodal forces. This equation can now be linearized employing a Taylor series about a known solution and expanding $\boldsymbol{\varphi}_{res}$. Not considering the second order terms, the result is

$$\boldsymbol{\varphi}_{res}(\mathbf{q} + \partial \mathbf{q}, \mathbf{p} + \partial \mathbf{p}) = \boldsymbol{\varphi}_{res}(\mathbf{q}, \mathbf{p}) + \frac{\partial \boldsymbol{\varphi}_{res}}{\partial \mathbf{q}} \delta \mathbf{q} + \frac{\partial \boldsymbol{\varphi}_{res}}{\partial \mathbf{p}} \delta \lambda \mathbf{p}_{ref} = 0 \quad (4.24)$$

where the tangent stiffness matrix is $\mathbf{K}_T = \frac{\partial \boldsymbol{\varphi}_{res}}{\partial \mathbf{q}}$ and $-\frac{\partial \boldsymbol{\varphi}_{res}}{\partial \mathbf{p}}$ is equal to the identity matrix \mathbf{I} . λ is the rate of change of the load of which it has been assumed the vector of the reference loadings \mathbf{p}_{ref} changes (meaning $\mathbf{p} = \lambda \mathbf{p}_{ref}$).

Eq. 4.24 can be rewritten, in a more compact form, as

$$\mathbf{K}_T \partial \mathbf{q} = \partial \lambda \mathbf{p}_{ref} - \boldsymbol{\varphi}_{res} \quad (4.25)$$

As λ is considered as a variable, in order to solve the system an additional equation is required. This governing equation is given by a constraint relation $c(\partial \mathbf{q}, \partial \lambda)$; the system then finally becomes

$$\begin{cases} \mathbf{K}_T \partial \mathbf{q} = \partial \lambda \mathbf{p}_{ref} - \boldsymbol{\varphi}_{res} \\ c(\partial \mathbf{q}, \partial \lambda) = 0 \end{cases} \quad (4.26)$$

Different incremental schemes can be employed by changing the constraint equation; for instance, if the equation is $\partial \lambda = 0$, the above system uses a load control method. If, on the contrary, if the equation is $c(\partial \mathbf{q}, \partial \lambda) = \partial \mathbf{q} = 0$, the system corresponds to a displacement control method.

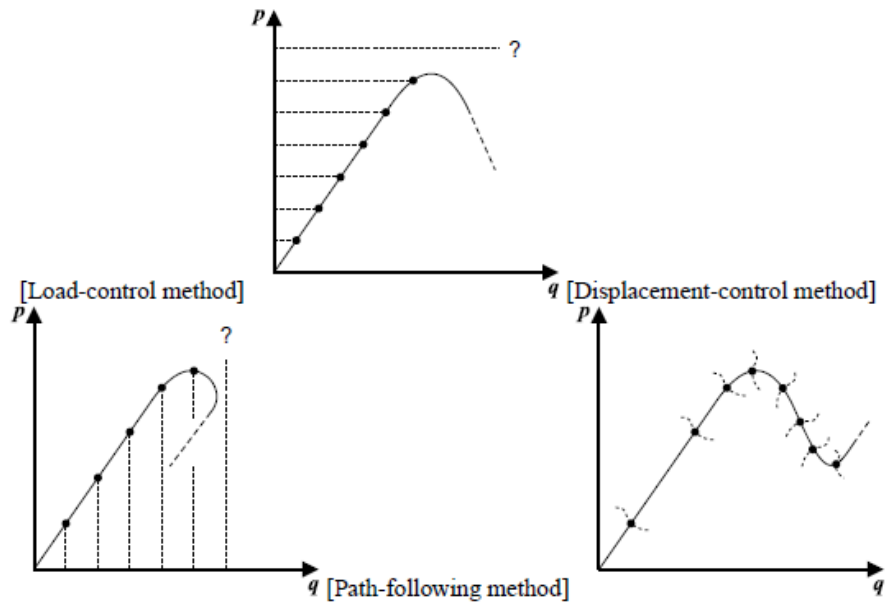


Figure 4.4: Different representations of the constraint equation located in Eq. 4.26 [24]

From now on, a path-following method will be employed, in which both the constraint equation depends both on displacement and load parameter variations. Differences between these three methods can be graphically appreciated in Fig. 4.4, and a more in depth discussion can be found in [28].

Chapter 5

Examples of Nonlinear Problems using the *MUL*² Software

This chapter aims to showcase the capabilities of the *MUL*² software, with particular regard to geometrically nonlinear problems, briefly showcasing some results obtained in order to demonstrate its reliability. The main objective was to replicate some fundamental results of nonlinear analyses as reported in [29] and [24].

In particular, the first section deals with the large deformations of a simple beam subjected to a tip loading as defined in Fig. 5.1. The resulting u_z deformations for different \mathbf{b}_{nl} contributions are reported in Fig. 5.2.

The second section instead focuses on the post-buckling behaviour of the same beam subjected to a compressive load. The unstable solution branches represented in the results have been enforced by applying a small load defect d (Fig. 5.4 and Fig. 5.5). The material for all the analyses performed in this report is set as Al 6061-T6, with the following mechanical properties: $E = 69.8$ GPa, $\nu = 0.33$ and density $\rho = 2700 \frac{\text{kg}}{\text{m}^3}$.

5.1 1D Structures Analyses

In this first section, analyses of 1D structural models will be performed in order to showcase the versatility and accuracy of the software. The 1D structure that will be considered is a classical cantilever beam, for which exact solutions are present extensively in the literature [30]. This allows the results to be confronted with a widely accepted benchmark. It will be shown how the *MUL²* results accurately approximate the exact solution with a limited required computational cost.

The study has been carried out for both slender and thick beams. The u_y and u_z deformations are reported for these cases.

Before showcasing the results, a simple convergence analysis has been performed in order to select the most suitable mesh for the following analyses. The obtained results for three different 1D meshes (5B4, 10B4 and 20B4) have been compared with the classical Euler-Bernoulli analytic solution derived from the *elastica* expression, defined as:

$$u_z = \frac{PL^3}{3EI} = \frac{PL^3}{3E} \frac{12}{h^4} = \frac{50 \cdot 100^3}{3 \cdot 69.8 \cdot 10^9} \frac{12}{1^4} = 0.29028 \cdot 10^{-2} \text{ m} \quad (5.1)$$

In Table 5.1, the vertical tip displacements u_z for the three compared meshes are reported; the relative error percentage between the exact Eulero-Bernoulli solution and the results is also reported. From this convergence analysis, the 10B4 mesh has been selected even if the 20B4 is more accurate with respect to the exact solution. This choice stems from a compromise between accuracy of the solution and the required computational cost; so a coarser but adequately accurate mesh has been chosen for the subsequent studies.

MESH	5B4 (1Q9)	10B4 (1Q9)	20B4 (1Q9)
u_z			
Value [m]	$0.286719 \cdot 10^{-2}$	$0.286719 \cdot 10^{-2}$	$0.286719 \cdot 10^{-2}$
Err %	1.23 %	0.6 %	0.29 %

Table 5.1: Convergence analysis of u_z for three different meshes

5.1.1 Geometric Nonlinearities in a Beam Structure

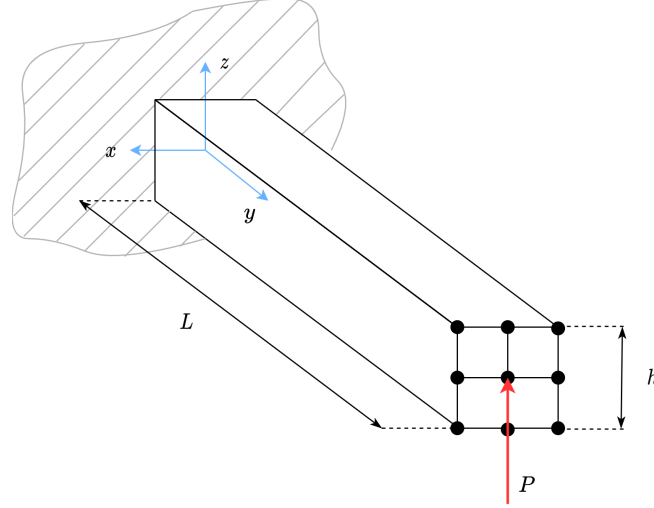


Figure 5.1: Beam geometry, cross-sectional mesh and representation of the load

The aforementioned beam has been subdivided into 10B4 unidimensional elements along the y -axis, while the cross-section has been discretized as 1Q9 elements, as reported in Fig. 5.1. In this first iteration, the aspect ratio $\frac{L}{h}$ has been set to 10, as $L = 100$ mm and $h = 10$ mm. The load is applied in the center node of the last section of the beam, as reported in the figure, and was defined as $P_0 = 50$ N.

Given a three dimensional displacement field $\mathbf{u}(x, y, z) = \{u_x \ u_y \ u_z\}^T$, the Green-Lagrange strain components can be defined as follows:

$$\boldsymbol{\varepsilon} = \boldsymbol{\varepsilon}_l + \boldsymbol{\varepsilon}_{nl} = (\mathbf{b}_l + \mathbf{b}_{nl})\mathbf{u} \quad (5.2)$$

where $\boldsymbol{\varepsilon}$ is the vector of the strain components and \mathbf{b}_l and \mathbf{b}_{nl} are the linear and nonlinear differential operators matrices. For a more in-depth look inside the theory behind the CUF/FEM code integration, the reader is referred to Chapter 4.

As an input in the nonlinear analysis, the software allows for various geometrical nonlinear approximations. For instance, in Fig. 5.2, four different approximations have been computed and reported: the fully nonlinear case (blue line, all contributions of the \mathbf{b}_{nl} matrix are considered), a less conservative nonlinear case (blue dash-dotted line), the 2D Von Karman solution (red dash-dotted line) and the linear case (red dashed line, all contributions of the nonlinear differential matrix are neglected).

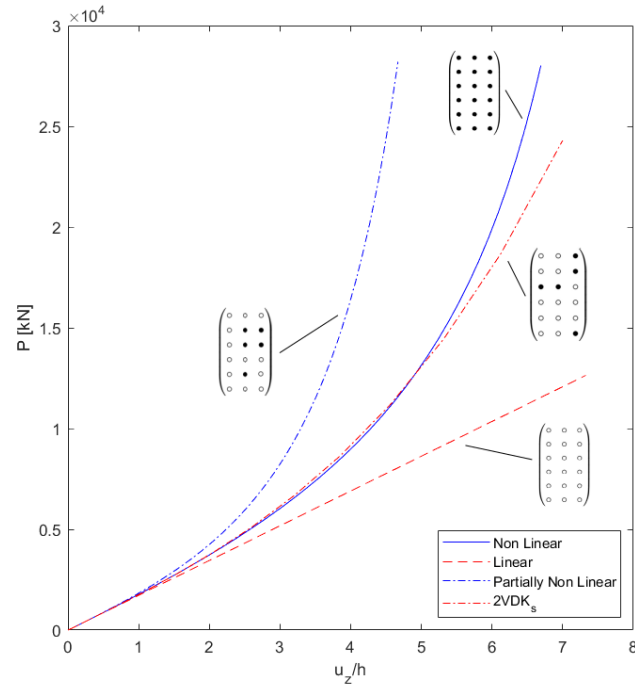


Figure 5.2: Equilibrium curves of a cantilever square beam for different nonlinear approximations of a beam with aspect ratio $\frac{L}{h} = 10$

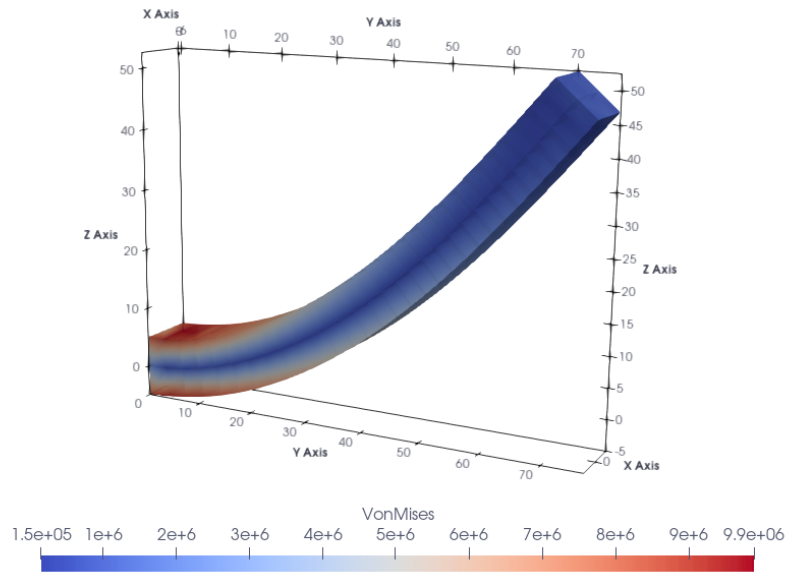


Figure 5.3: Von Mises stresses and deformed shape of the beam (fully nonlinear solution)

The trends of the reported equilibrium curves is consistent with those reported in [29].

For the sake of completeness, the Von Mises stresses and displacement of the fully nonlinear solution are reported in Fig. 5.3.

5.1.2 Post Buckling in a Beam Structure

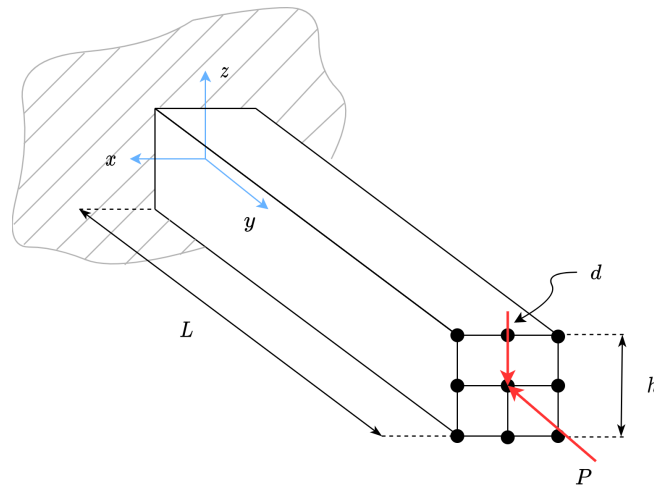


Figure 5.4: Beam geometry, cross-sectional mesh and representation of the loads

As already reported in the first part of the chapter, the post-buckling behaviour of the same beam has been studied using a full nonlinear approximation using the Green-Lagrange strain components. The compressive load has been set to $P_0 = 50$ N and the load defect to $d = 0.02 \cdot P_0$.

First, in Fig. 5.5a, the post-buckling equilibrium curve of a thick beam (aspect ratio $\frac{L}{h} = 10$) is reported; meanwhile, in Fig. 5.5b, a similar result for a slender beam ($\frac{L}{h} = 100$) is evaluated.

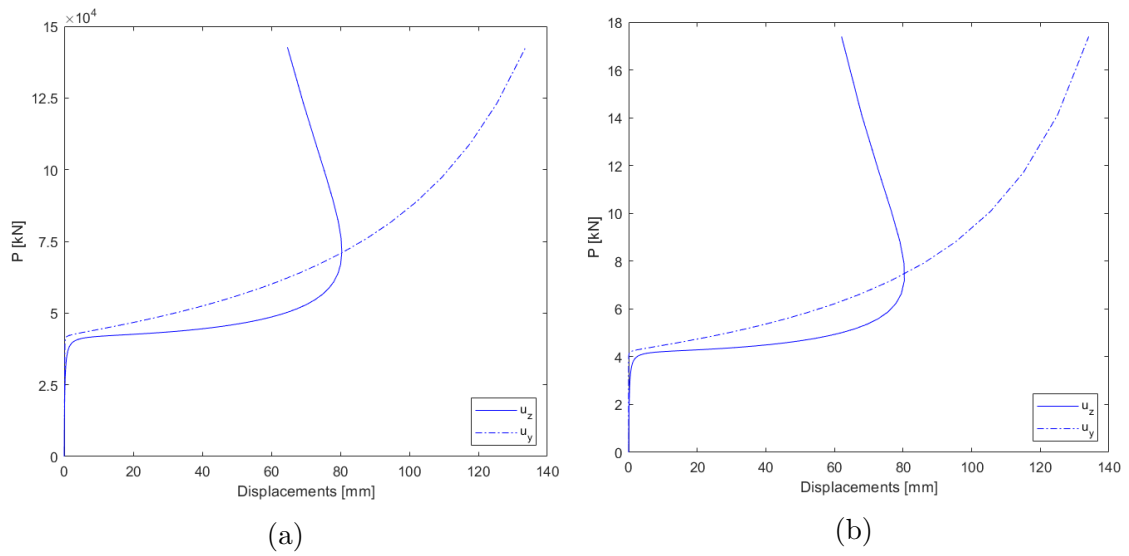


Figure 5.5: Post-buckling equilibrium curves for a thick ($L/h = 10$, Fig. 5.5a) and slender ($L/h = 100$, Fig. 5.5b) cantilever square beam

5.2 2D Structures Analyses

In the second part of the chapter, the objective is to showcase some results from two-dimensional structures for completeness. Studying initially these types of structures (even if on a surface level) is key, as 2D cylindrical shells are the focal point of the studies in this thesis work.

The first section will focus on a modal analysis performed on a simply supported plate, in which the first 10 natural frequencies are reported, along with some deformed shapes at the resonant frequencies.

The last section will focus on a fully nonlinear analysis of a hinged shell with an applied load at the center. The obtained results will be compared with the ones obtained in [23].

5.2.1 Modal Analysis of a 2D Plate

The first 10 natural frequencies of the free vibration analysis (103) performed on the aforementioned plate are reported in Table 5.2. In Fig. 5.6, the deformed shapes of the first four frequencies are presented. The plate has been modelled with a 10x10Q9 mesh, while the cross section with 1B3 elements.

Mode #	Frequency [Hz]
1	92.5
2	203.1
3	232.8
4	339.6
5	402.1
6	460.1
7	532
8	565
9	698.6
10	751.5

Table 5.2: First ten natural frequencies (10x10Q9 mesh, 1B3 cross-section)

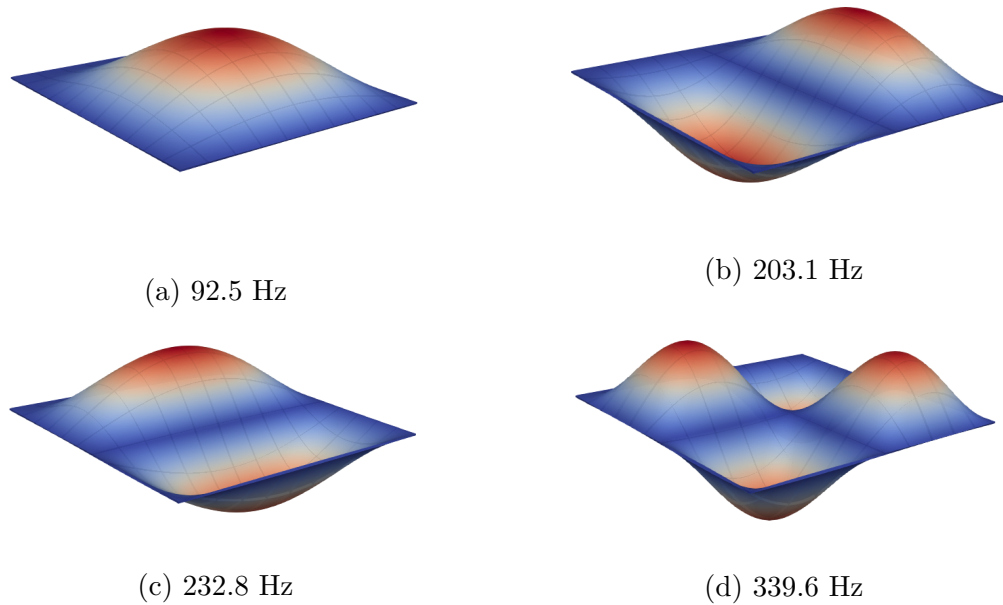


Figure 5.6: Deformed shape of the first four natural frequencies

5.2.2 Nonlinear Analysis of a Shell Structure

For this section, a fully nonlinear analysis of shell structure was performed. The shell has been discretized with a 10x10Q9 mesh, while the thickness has been modelled with 1B3 elements.

The applied load of $P_0 = 200$ N was applied at the center of the shell, as previously stated. Two of the edges of the shell have been hinged.

The equilibrium curve resulting from a full nonlinear analysis is reported in Fig. 5.7. This result is coherent with the trend reported in [23].

Finally, in Fig. 5.8, three deformed shapes (and displacement values in millimeters) of the shell during the nonlinear analysis are reported. These results are coherent with the ones reported in [23] as well.

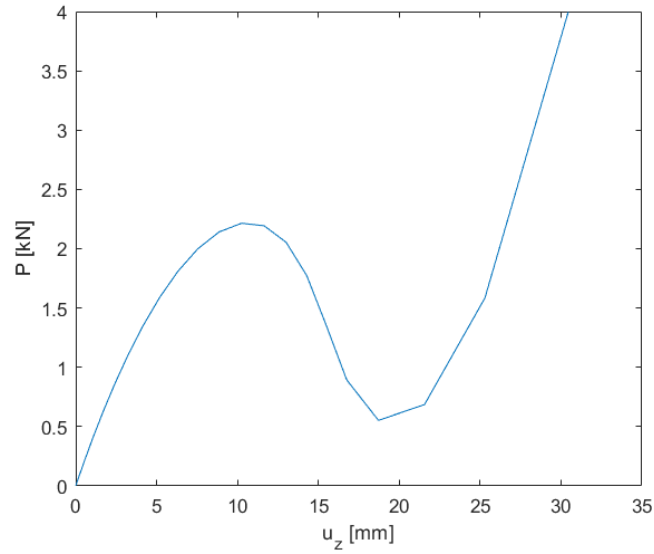


Figure 5.7: Equilibrium curve of a shell for a fully nonlinear solution (the displacement is evaluated at the center of the structure); 10x10Q9 mesh, 1B3 cross-section

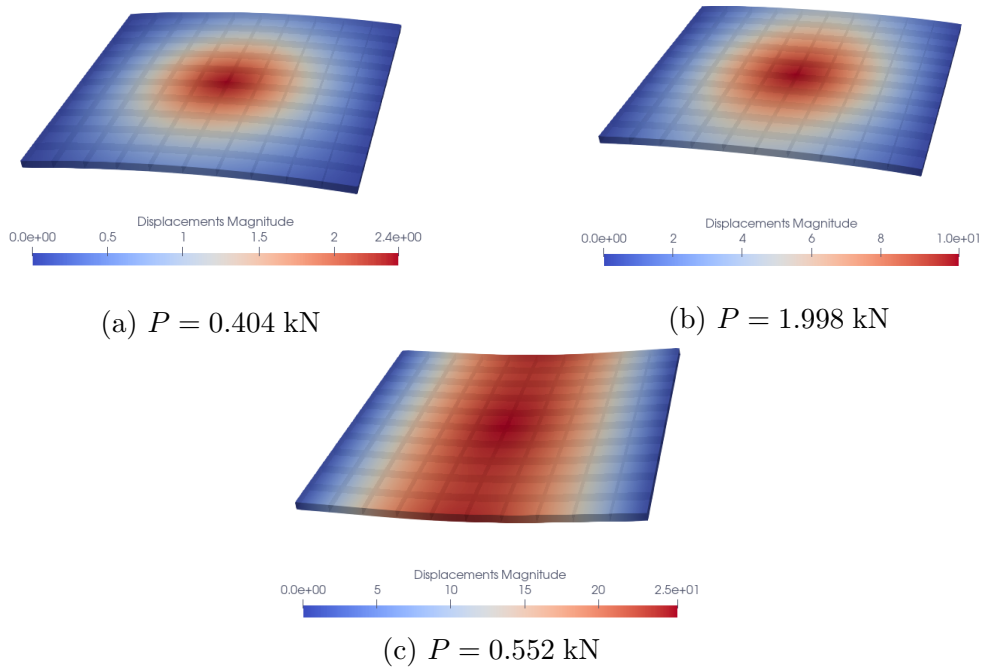


Figure 5.8: Deformed shapes for three different equilibrium states

5.2.3 Pinched Semi Cylindrical Shell

An interesting structural analysis of a thin-walled semi-cylindrical shell is presented in [23]. In this work, a full nonlinear analysis is executed using the CUF and the MUL^2 software; the results are then compared with the benchmark of the analysis reported in [31], in which the popular commercial FEM software ABAQUS is used.

In this model, the semi cylindrical shell is clamped and subjected to a concentrated load at the free end (as reported in Fig. 5.9). Also in the analysis, the adopted material is an isotropic aluminum alloy, while the geometrical dimensions are $L = 3.048$ m as the length, $R = 1.016$ m as the radius of the cylinder and $h = 0.03$ m as the thickness of the metal sheet.

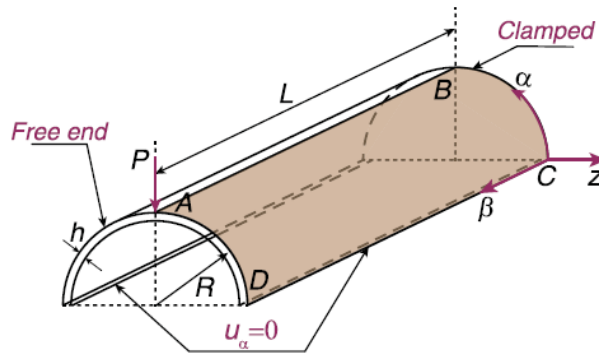


Figure 5.9: Schematic diagram of the thin-walled semi cylindrical shell model with a concentrated load [23]

The clamped boundary condition is imposed by $u_\alpha = u_\beta = u_z = 0$ at $\beta = 0$; the circumferential deflections are constrained along the longitudinal edges by imposing $u_\alpha = 0$ at $\alpha = 0$ and $\alpha = \pi R$.

The concentrated load is applied at point A as presented in Fig. 5.9.

The first step reported in [23] is a convergence analysis of the aforementioned shell model, in which different finite element approximations are tested in order to determine the most efficient one in terms of computational cost and results accuracy. The reader is redirected to the paper if interested in the full analysis. The results of this convergence analysis can be appreciated by the comparison of large deflection nonlinear curves for this structure reported in Fig. 5.10a.

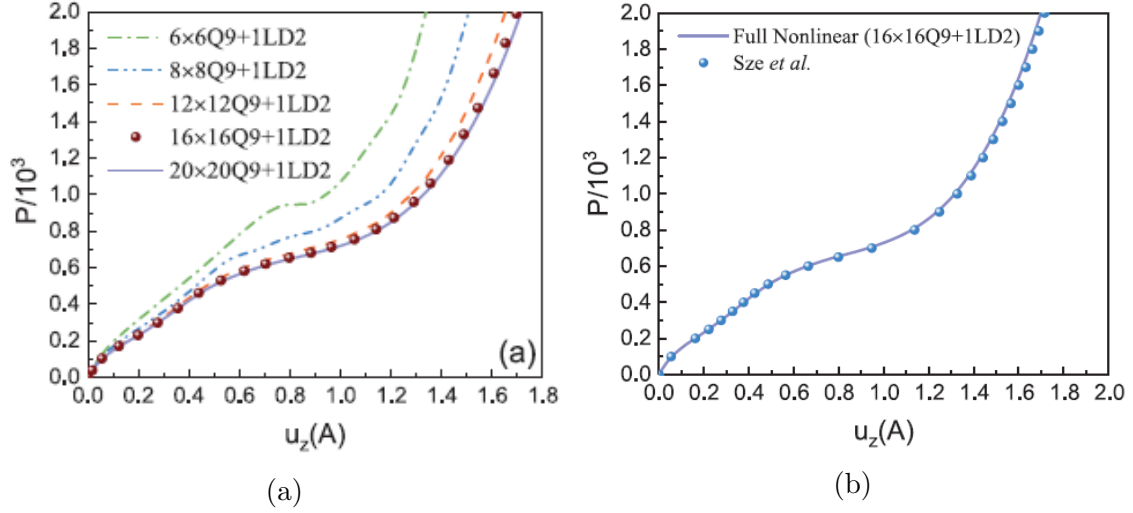


Figure 5.10: Convergence analysis of the model with a comparison between different in-plane meshes (5.10a, [23]); nonlinear equilibrium curve of the model using a 16x16Q9+1LD2 mesh compared with the results in [31] (5.10b, [23])

It has been found that the best convergence of results occurs when considering a 16x16Q9 in-plane mesh; regarding which Lagrangian Expansion (LE) functions for the thickness direction, at least LD2 kinematics should be considered to predict large deflections. Therefore, the considered finite element model in the analysis, along with the resulting equilibrium curve, is presented in Fig. 5.10b, as the large deflection behaviour of the structure is accurately captured, and with less computational cost required as well.

The resulting solution of the CUF is confronted with the results of [31] which is taken to be a reference solution in order to benchmark the accuracy of the FEM model. In this paper, 40x40 S4R four node shell elements were considered and ABAQUS was used for the analysis. As can be seen in Fig. 5.10b, the results given by the CUF model is appropriately accurate in predicting the large deflection behaviour of the structure.

To complete the argument, some typical deformed configurations of three equilibrium states of the shell structure are reported in Fig. 5.11, in which the initial undeformed structure is reported for comparison.

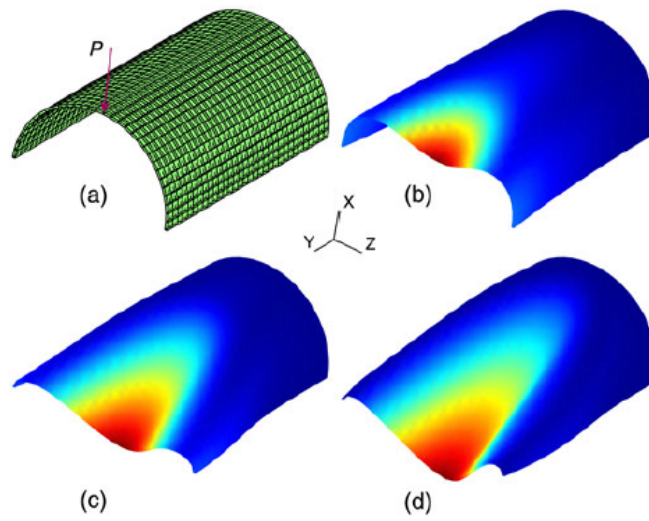


Figure 5.11: The initial undeformed structure and three deformed configurations of the semi cylindrical shell model for three equilibrium states [23]

Chapter 6

Conclusions and Recommendations

As it becomes more obvious that, in order to maintain a certain level of competitiveness in the current space transportation market, reusable launch vehicle design has become an integral and inviting part of any new launcher program, both in the public sector (national space agencies) and in the private sector (e.g. SpaceX and Blue Origin). The reusability and cost effectiveness factors for any new launcher should be investigated and should improve upon the successes and shortcomings of past and current RLVs.

More and more demand for space transportation applications is emerging, from the legacy practices of unmanned orbital launches (satellites, cargo missions to space stations) to the exciting new tourism-based space economy, and it's only going to grow exponentially in the coming years and decades.

The development of successful reusable launch vehicle program is strictly tied to technological advancements and new materials developments. Numerous solutions have been proposed, designed and are now operating, mainly reusable stages of multistage rockets. Reusable single stage to orbit vehicles, like the Space Shuttle and

the X-33 prototype, demonstrated the feasibility of such solutions for manned space transportation to orbit but not without shortcomings. In fact, a lot of structural problems restricted the effectiveness of such vehicles due to high downtime between missions and unpredictably high maintenance and refurbishment costs, both in monetary and manpower terms.

These aspects could be improved. The main structural weak areas that could favour from new materials, techniques and technological research were discussed in the previous chapter. Among them, the main structure of the vehicle itself could improve reusability factors with the use of lighter materials, even if more costly and difficult to produce due to their inherent nature and the extensive need for testing campaigns, like graphite-epoxy composite materials or graphite-BMI composite materials, which are capable of sustaining higher temperatures that inevitably occur during atmospheric reentry.

Other proposed improvement areas include the development of reliable cryogenic tanks. These are needed when considering a LOX/LH₂ fuel configuration design, as present in many expendable RLVs. Two main material configurations are considered: aluminum-lithium metallic alloy or composite materials. Metallic alloys have been widely used as thin-walled structures of tanks over the years, and present many advantages when cryogenic fuels are considered. New metallic materials bring a reduction in weight and improved mechanical strength, and could be prime candidates in use in liquid oxygen tanks. On the other hand, composite materials are known for optimal strength-to-weight ratios, but fall short in crack prevention due to high velocity impacts and subsequent repairability considerations. Despite this, with the right cryoinsulation, they have shown to have no leakage at nominal pressures and no permeability or cracking during extensive cycle testing. Thanks to their low weight with respect to their strength, and after having been successfully tested and validated for use with cryogenic fuels, they have become prime candidates for use in cryogenic LH₂ tanks.

Finally, one of the most important areas of development of RLVs are thermal protection systems (TPS). From the experience gathered from the Space Shuttle, many research programs on new and improved materials for thermal protection have been investigated, both for the extreme thermal radiation on the external surfaces of the vehicle and for the effective insulation of cryogenic fuel in tanks. Among the prime candidates, composite materials have been proposed, like for example

composite refractory TPS (C/SiC), which present good resistance to atmospheric conditions (rain, hail, frost and particle impacts) and reduced weight compared to the ceramic tiles used in the Space Shuttle. Ceramic matrix composites (SiC/SiC and ACC) are of interest, as they can protect the most thermally stressed parts of the vehicle up to 1650°C, also weighting less than ceramic tiles.

Metallic TPS have also been introduced, which exhibit lower weight, higher reliability, better durability and lower total periodic costs with respect to ceramic tiles. Among them, nickel based superalloys and titanium based superalloys are prime examples; multilayer composites can be introduced into these metallic materials to improve high temperature properties; using intermetallics as a toughener, high temperature strength and creep resistance are maintained through a wide range of operative temperatures.

Still more research and testing is needed to validate all solutions proposed, but with constant technological advancements, the future reusable launch vehicles could be more affordable, more efficient and, in turn, lower launch costs for customers, commercial or private as they may be, reducing the access-to-space overall cost.

Bibliography

- [1] E. Britannica. “Launch vehicle”. (2019), [Online]. Available: <https://www.britannica.com/technology/launch-vehicle>.
- [2] R. Wagner, “Robust design of buckling critical thin-walled shell structures”, Ph.D. dissertation, 2019.
- [3] V. Weingarten and P. Seide, “Sp-8019 - buckling of thin-walled truncated cones”, NASA Langley Research Center, 1968.
- [4] M. W. Hilburger, M. C. Lindell, W. A. Waters, and N. W. Gardner, “Test and analysis of buckling-critical stiffened metallic launch vehicle cylinders”, in *2018 AIAA/ASCE/AHS/ASC structures, structural dynamics, and materials conference*, 2018, p. 1697.
- [5] V. Krasovsky, V. Marchenko, and R. Schmidt, “Deformation and buckling of axially compressed cylindrical shells with local loads in numerical simulation and experiments”, *Thin-walled structures*, vol. 49, no. 5, pp. 576–580, 2011.
- [6] A. Y. Evkin, “Local buckling of cylindrical shells. pogorelov’s geometrical method”, in *Problems of Nonlinear Mechanics and Physics of Materials*. Springer International Publishing, 2019, pp. 369–391.
- [7] “Spacecraft design loads”, in *Spacecraft Structures*. Springer Berlin Heidelberg, 2008, pp. 27–69.
- [8] SpaceX, “Falcon user’s guide”, 2020.
- [9] M. Sippel, S. Stappert, J. Wilken, N. Darkow, S. Cain, S. Krause, T. Reimer, C. Rauh, D. Stefaniak, T. Thiele, *et al.*, “Focused research on rlv-technologies: The dlr project akira”, 2019.
- [10] S. Stappert, J. Wilken, L. Bussler, and M. Sippel, “A systematic comparison of reusable first stage return options”, 2019.

- [11] BlueOrigin, “New glenn payload user’s guide”, 2018.
- [12] S. Stappert, J. Wilken, and M. Sippel, “Evaluation of european reusable vtvl booster stages”, in *2018 AIAA SPACE and Astronautics Forum and Exposition*, 2018, p. 5239.
- [13] N. R. Council *et al.*, “Reusable booster system: Review and assessment”, 2013.
- [14] N. R. Council, *Reusable Launch Vehicle: Technology Development and Test Program*. The National Academies Press, 1995.
- [15] R. Wanhill, “Chapter 15 - aerospace applications of aluminum–lithium alloys”, in *Aluminum-lithium Alloys*, N. Eswara Prasad, A. A. Gokhale, and R. Wanhill, Eds., Boston: Butterworth-Heinemann, 2014, pp. 503–535.
- [16] NASA. “Nasa tests game changing composite cryogenic fuel tank”. (2013), [Online]. Available: https://www.nasa.gov/content/nasa-tests-game-changing-composite-cryogenic-fuel-tank_marshall_news.
- [17] CompositesWorld. “Composite pressure vessels take on cryogenic temperatures”. (2018), [Online]. Available: <https://www.compositesworld.com/articles/composite-pressure-vessels-take-on-cryogenic-temperatures>.
- [18] D. Zhang, G. Chen, and J. Han, “Research on new materials of metallic thermal protection system panel for reusable launch vehicle”, *2006 1st International Symposium on Systems and Control in Aerospace and Astronautics*, pp. 5–412, 2006.
- [19] E. Carrera, M. Cinefra, M. Petrolo, and E. Zappino, *Finite element analysis of structures through unified formulation*. John Wiley & Sons, 2014.
- [20] E. Carrera, “A class of two dimensional theories for multilayered plates analysis”, *Atti Accademia delle Scienze di Torino*, vol. 19-20, pp. 49–87, 1995.
- [21] D. Kim and R. A. Chaudhuri, “Full and von karman geometrically nonlinear analyses of laminated cylindrical panels”, *AIAA journal*, vol. 33, no. 11, pp. 2173–2181, 1995.
- [22] B. Wu, A. Pagani, M. Filippi, W. Chen, and E. Carrera, “Large-deflection and post-buckling analyses of isotropic rectangular plates by carrera unified formulation”, *International Journal of Non-linear Mechanics*, vol. 116, pp. 18–31, 2019.

- [23] B. Wu, A. Pagani, W. Chen, and E. Carrera, “Geometrically nonlinear refined shell theories by carrera unified formulation”, *Mechanics of Advanced Materials and Structures*, pp. 1–21, 2019.
- [24] A. Pagani and E. Carrera, “Unified formulation of geometrically nonlinear refined beam theories”, *Mechanics of Advanced Materials and Structures*, vol. 25, no. 1, pp. 15–31, 2018.
- [25] A. Pagani and E. Carrera, “Large-deflection and post-buckling analyses of laminated composite beams by carrera unified formulation”, *Composite Structures*, vol. 170, pp. 40–52, 2017.
- [26] E. Carrera, A. Pagani, R. Augello, and B. Wu, “Popular benchmarks of nonlinear shell analysis solved by 1d and 2d cuf-based finite elements”, *Mechanics of Advanced Materials and Structures*, pp. 1–12, 2020.
- [27] E. Carrera and M. Petrolo, “Refined beam elements with only displacement variables and plate/shell capabilities”, *Meccanica*, vol. 47, no. 3, pp. 537–556, 2012.
- [28] E. Carrera, “A study on arc-length-type methods and their operation failures illustrated by a simple model”, *Computers and Structures*, vol. 50, no. 2, pp. 217 –229, 1994.
- [29] A. Pagani, E. Carrera, and R. Augello, “Evaluation of various geometrical nonlinearities in the response of beams and shells”, *AIAA Journal*, vol. 57, no. 8, pp. 3524–3533, 2019.
- [30] L. Euler, “De curvis elasticis”, *Lausanne and Geneva*, 1744.
- [31] K. Sze, X. Liu, and S. Lo, “Popular benchmark problems for geometric nonlinear analysis of shells”, *Finite elements in analysis and design*, vol. 40, no. 11, pp. 1551–1569, 2004.